Tracking molecular hydrogen migration along a subduction shear zone

Tracking molecular hydrogen migration along a subduction shear zone

Ritabrata Dobe[1], Francesco Giuntoli[1], Orlando Sebastien Olivieri[1], Guillaume Siron[2], Giulio Viola[1], Luca Menegon[3], and Alberto Vitale Brovarone[1,4,5]

[1]Dipartimento di Scienze biologiche, geologiche e ambientali, Alma Mater Studiorum, University of Bologna, Bologna, Italy

[2]Université de Franche-Comté, CNRS, CHRONO-E (UMR 6249), F-25000 Besançon, France

[3]Njord Centre, Department of Geoscience, University of Oslo, Oslo, Norway

[4]Institut de Minéralogie, de Physique des Matériaux et de Cosmochimie (IMPMC), Sorbonne Université, Muséum National d'Histoire Naturelle, Paris, France

[5]Institute of Geosciences and Earth Resources, National Research Council of Italy, Pisa, Italy

Abstract

This manuscript presents integrated field, petrographic, microstructural and thermodynamic modelling results documenting the high-pressure channelization of H_2 and the rheological impact of its reactivity with carbonate (dolomite and calcite)-rich rocks along a serpentinite-hosted shear zone from Alpine Corsica (France). Microstructures within the carbonates attest to the occurrence of a deformation continuum, evolving from initial brittle fracturing to strain localization by viscous deformation. Raman spectra of fluid inclusions within the carbonates reveals the circulation of H_2 and CH_4 at all stages of the microstructural evolution, the latter interpreted to be the result of H_2-carbonate interactions. Thermodynamic models suggest that carbonate phase stability at pressure-temperature conditions representative of a subduction setting is modified by the presence of H_2, with dolomite being progressively replaced by calcite+graphite+magnetite with increasing H_2 in the system. An initial phase of overpressure created by H_2-rich fluids led to the brecciation of dolomite, creating a fine-grained aggregate, which facilitated a switch to a semi-brittle mode of deformation and created high-permeability pathways for subsequent phases of H_2 infiltration. Subsequent phases of infiltration of H_2 were accompanied by transformation of dolomite to calcite, the degree of transformation dependent upon the efficiency of H_2 percolation. Calcite, being rheologically weaker than dolomite at these temperatures, underwent viscous flow in domains of extensive dolomite reduction, whereas adjacent dolomite-rich domains contain minimal imprints of extensive plastic deformation. Our results demonstrate extensive fossilized H_2-carbonate reactivity and show that the infiltration of H_2-rich fluids strongly affects the rheology of carbonates by inducing reactivity and phase transitions.

1. INTRODUCTION

Molecular hydrogen (H_2) has been touted to have substantial potential as green fuel, since the only byproduct of H_2 combustion is water (Osselin et al., 2022). Traditional methods of industrial H_2 fuel production by the electrolysis of H_2O are energy intensive processes and not environmentally sustainable in the long term (Osselin et al., 2022). Additionally, underground storage of H_2 in geologic reservoirs, while necessary to store requisite amounts of H_2 to alleviate forecasted global demand, is also challenging and requires an in-depth investigation into the reactivity between H_2 and rock-forming minerals (Braid et al., 2024). The recent discovery of voluminous naturally occurring resources of H_2 in the Earth's subsurface has necessitated a need to evaluate natural H_2 as a possible source of clean fuel (Prinzhofer et al., 2018; Osselin et al., 2022; Truche et al., 2024). Moreover, the natural geologic systems that host these resources also provide information on how H_2 interacts with rocks and minerals (Reeves and Seewald, 2024), and these paleo H_2-rock interactions can serve as proxies for underground hydrogen storage (UHS;Malki et al., 2024; Braid et al., 2024). In addition to its potential significance to the energy transition, H_2 plays an important role in planetary evolution and serves as source of energy for chemosynthetic life (McGlynn et al., 2020; Lappan et al., 2023; Gill-Olivas et al., 2023; Peverelli et al., 2024). Molecular hydrogen is also an important species in the deep Earth, and its concentration in the Earth's core is coupled with the oxidation of the residual mantle, thereby exerting a substantial control on the evolution of the redox state of the Earth's interior (Hirschmann et al., 2012).

The two most common sources of H_2 in the Earth's subsurface involve either the reduction of H_2O and concomitant oxidation of ferrous iron to ferric iron in minerals during water-rock interactions, such as serpentinization (Charlou et al., 2002; Sleep et al., 2004; Klein et

al., 2013), or the radiolytic dissociation of H_2O (Lollar et al., 2014). Although fluid-rock reactions that lead to the formation of H_2 at different crustal levels have been studied in some detail, the mechanisms by which H_2 migrates through the crust, as well as their effects on rock deformation, are relatively poorly understood. A recent study by Prinzhofer et al. (2024) documented high fluxes of H_2 and He along reactivated faults in the municipality of Maricà in Brazil. Similarly, high H_2 fluxes have been documented along a network of shallow fractures in the Bulqizë chromite mine in Albania (Truche et al., 2024). While these recent discoveries have been successful in linking extensive surficial fluxes of reduced fluids, such as H_2 and abiotic CH_4, to structural discontinuities, such as faults and fracture networks acting as preferential flow conduits, the structural, microstructural, mineralogical, and geochemical markers of H_2 percolation from potentially deeper source areas within the crust are still largely unexplored. Nevertheless, natural examples of H_2 circulation and channelization in orogenic belts have been recently documented and require more detailed investigations to provide insights into the geochemical and microstructural markers of natural H_2-rock interactions (Galvez et al., 2013; Vitale Brovarone et al., 2017; Prinzhofer et al., 2018; Giuntoli et al., 2020, 2024; Boutier et al., 2024; Truche et al., 2024).

High strain zones, such as faults and shear zones, can act as efficient conduits for fluid migration (Austrheim, 2013) and crustal H_2 may plausibly migrate preferentially along these structures. However, although numerous studies have focused on the role played by aqueous fluids in altering the rheology of the Earth's crust, the rheological changes induced by low fO_2 fluids rich in H_2 along deformation zones are relatively poorly constrained. Water-rich fluids generally lead to strain softening by promoting processes such as hydrolytic weakening, grain boundary sliding (GBS), dissolution-precipitation creep and the formation of rheologically weak

84 phases, such as phyllosilicates (Post and Tullis, 1998; Skemer et al., 2006; Fusseis et al., 2009,
85 2023; Getsinger et al., 2013; Menegon et al., 2015; Nicolas et al., 2016; Précigout et al., 2017;
86 Dobe et al., 2021). Only a few studies, on the other hand, have documented the structural and
87 microstructural imprints of natural H_2-rock interactions (Giuntoli et al., 2020, 2024). Most of
88 what we know on the effect of H_2 on material properties is thus derived from metallurgical and
89 material science literature, pertaining to processes such as stress corrosion cracking during H_2
90 injection and H_2 embrittlement (Barnett and Kerrich, 1980; Scully et al., 2012; Robertson et al.,
91 2015; López Freixes et al., 2022). This is largely due to the fact that H_2 interactions with many
92 crustal minerals may not produce marked reaction products and the identification of its paleo-
93 circulation in crustal rocks is still challenging.
94 Carbon-bearing minerals, such as carbonates and graphite, are common in many crustal
95 settings and may be extremely reactive with H_2 (Malvoisin et al., 2012; Galvez et al., 2013;
96 Lazar et al., 2014; Vitale Brovarone et al., 2017; Giuntoli et al., 2020; Peng et al., 2021; Peña-
97 Alvarez et al., 2021; Gelencsér et al., 2023; Huang et al., 2024; Braid et al., 2024; Harada and
98 Tsujimori, 2024; Zhang et al., 2024), and may attest to the circulation of reduced fluids enriched
99 in H_2 (Peverelli et al., 2024; Boutier et al., 2024; Giuntoli et al., 2024). These minerals and their
100 microstructural evolution may therefore be used to track H_2 infiltration and to assess the effects
101 of its percolation at crustal conditions.
102 We studied the microstructural and petrological evolution of carbonate rocks associated
103 with a serpentinite-hosted shear zone from Alpine Corsica (France) to track H_2 infiltration. A
104 combination of optical microscopy, cathodoluminescence (CL) observations and Scanning
105 Electron Microscopy (SEM) in conjunction with Electron Dispersive Spectroscopy (EDS)
106 reveals the presence of multiple carbonate generations in this suite of rocks, which are

chemically and microstructurally heterogeneous, and Raman spectra of fluid inclusions within the different carbonate generations testify to the abundant circulation of H_2 through these lithologies. Electron Backscatter Diffraction (EBSD) analyses from different microstructural domains were performed to gain insights into the strain accommodation mechanisms within the different carbonate generations and understand the role played by H_2 in developing the observed microstructural heterogeneity; thermodynamic models of H_2-carbonate interactions show that H_2 influx within carbonates at pressure-temperature conditions relevant for subduction zones induced phase transitions between carbonate phases with drastically different rheological properties. By integrating our results from the aforementioned analyses and models, we aim to provide new insights into rheological changes induced by H_2 circulation and reactivity, with an emphasis on the nature of deformation induced by phase transitions caused by H_2-rock interactions and into the definition of characteristic markers of H_2 circulation and reactivity in the crust.

1.1 Geologic setting

The island of Corsica can be subdivided into two major tectonometamorphic domains (Fig. 1A), namely Hercynian Corsica to the west and southwest, and Alpine Corsica to the northeast (Malavieille et al., 1998; Vitale Brovarone et al., 2011, 2013; Molli and Malavieille, 2011; Vitale Brovarone and Herwartz, 2013; Di Rosa et al., 2020a; Rossetti et al., 2023). Hercynian Corsica is dominantly granitic and was mostly unaffected by the Alpine orogeny, except for a marginal transition zone, the so-called parautochthonous units, that underwent Alpine metamorphism and deformation at low-grade blueschist to greenschist facies conditions (see below; Molli et al., 2017; Di Rosa et al., 2020c, 2020b).

Alpine Corsica represents an exhumed orogenic wedge consisting of ocean- and continent-derived units (Vitale Brovarone et al. 2013 and references therein). It comprises three main domains: the continental margin units or the parautochthonous units, the oceanic units of the Schistes Lustrés and the weakly metamorphosed turbidites and ophiolites of the Nappes Supérieures (Molli, 2008; Molli and Malavieille, 2011; Malusà et al., 2015). The parautochthonous units represent fragments of the Hercynian Corsica basement and their sedimentary cover sequence overprinted during the Alpine orogeny up to blueschist-facies conditions at about 46.7±0.6 Ma to 34.4±0.8 Ma (Brunet et al., 2000; Martin et al., 2011).

The Schistes Lustrés are composed of metamorphosed oceanic rocks (variably serpentinized peridotites, metagabbros, metabasalts) and metasedimentary cover along with slivers of continental basement collectively referred to as the "internal continental unit" (Cohen et al., 1981). The tectonic juxtaposition of oceanic and continental basement rocks is interpreted to have originated during rifting and extension of the Piemonte-Ligurian basin in pre-Alpine time (Vitale Brovarone et al., 2011; Beltrando et al., 2014). The Schistes Lustrés can be subdivided into three main tectonometamorphic units from west to east: a lawsonite-blueschist facies metasediment-rich zone, a lawsonite-eclogite facies meta-ophiolite-rich zone, and a lawsonite blueschist-facies zone (Vitale Brovarone et al., 2013), which are characterized by meta-ophiolites, continental slivers and associated metasediments that are distinguished on the basis of consistent tectonostratigraphic and metamorphic features and which show a metamorphic overprint from low-grade blueschist to lawsonite eclogite-facies conditions (Lahondere and Lahondere, 1988; Ravna et al., 2010; Vitale Brovarone et al., 2014; Beltrando et al., 2014). Peak metamorphic conditions are constrained at about 35 Ma in the lawsonite eclogite unit by U-Pb zircon and Lu-Hf garnet geochronology and around 37 Ma in the blueschist-facies unit by Lu-Hf

152 geochronology (Martin et al., 2011; Vitale Brovarone and Herwartz, 2013). The Nappes
153 Supérieures consist of a subgreenschist facies association of oceanic rocks and rocks of
154 continental affinity that experienced both brittle and ductile deformation. The present-day
155 structural position of the Nappes Supérieures atop of the Schistes Lustrés and the
156 Parautochthonous Hercynian units is the result of normal faulting related to the overthickened
157 antiformal stacking of Alpine Corsica and the opening of the Tyrrhenian basin (Jolivet et al.,
158 1998; Malavieille et al., 1998; Molli and Malavieille, 2011).

159 This study focuses on the hitherto undescribed Negru Shear Zone (NSZ hereafter) located
160 inside the Schistes Lustrés complex (Fig. 1B). The NSZ is located along the west coast of Cap
161 Corse, a few hundred meters north of the Negru beach, and deforms the lawsonite-eclogite
162 tectonometamorphic unit after Vitale Brovarone et al. (2013). In this domain, the lawsonite-
163 eclogite unit is primarily composed of ultramafic (variably serpentinized peridotites and
164 serpentinites), and mafic (metabasalts and metagabbros) lithologies, with subordinate
165 metasedimentary and continental basement slices. Peak metamorphic temperatures for this area
166 were estimated in metasedimentary rocks by means of Raman spectroscopy on carbonaceous
167 material at about 430º-470 °C (Vitale Brovarone et al., 2013) and pressure-temperature estimates
168 from mafic rocks, belonging to the same tectonometamorphic unit to the south, point to peak
169 metamorphic conditions in the range of 470-520 °C and 2-2.2 GPa (Ravna et al., 2010; Vitale
170 Brovarone et al., 2011).

171 **1.2 Field relations**

172 The NSZ is located inside a large, ~4x4 km body of serpentinite and is well exposed
173 along a roadcut (Figs. 2A&B). The shear zone is characterized by a high-strain domain, up to ~5
174 m thick, affecting metasomatized metasediments and metagabbros separating two comparatively

lower-strain blocks of serpentinite (Figs. 2A&B). The high-strain domain of the NSZ mainly formed within and at the expense of rock types that are currently sandwiched between the two serpentinite blocks. Large lenses of these rocks, up to 5 m thick, are preserved inside the high-strain domain and consist of variably metasomatized metagabbroic rocks –possibly autochthonous inside the serpentinized mantle section– and allochthonous rocks of metasedimentary origin. High-strain bands wrap around these lenses and generally exhibit higher strain in light-colored, metagabbro-derived domains. These intensely sheared bands are marked by a generally shallow (~12°) SW-dipping foliation and a down-dip stretching lineation. The lower-strain domains in the adjacent serpentinite blocks are characterized by a generally massive, yet locally foliated structure. Besides a first meter of intensely sheared serpentinite in contact with the high-strain domain, the structure of the serpentinite blocks is more complex and characterized by internally variable foliated domains wrapped in intensely sheared domains. The internal foliation dips shallowly (~6º-14º) to the SW away from the high strain zones and becomes progressively parallelized to the high strain zones, in their vicinity. The lower (footwall) serpentinite block is not well exposed, and the following description refers to the upper serpentinite block (hanging wall). The NSZ is cut at a low angle by a later brittle normal fault dipping c. 10° to the NW and associated with c. 10°-plunging slickenlines. The fault has a visible strike-length of 100 m (Figs. 2A&B). In the northwestern part of the roadcut, the fault is parallel to the base of the upper serpentinite block. Indurated gouges and light-colored carbonate-silica veins decorate the fault core and the immediate damage zone. These late-stage brittle structures will not be further described in this manuscript.

The first few meters of serpentinites above the high-strain domains are crosscut by a network of carbonate veins and anastomosing carbonate-rich deformation bands (Figs. 2C&D)

198 that preserve a continuum of deformation imprints from brittle to ductile. These carbonate veins
199 were not observed farther into the upper serpentinite block to the north and thus appear to be
200 genetically related to shearing within the high-strain domain.
201 On the weathered surfaces the vein network is seen to comprise an earlier set of brown to
202 dark gray colored carbonate veins, and a later set of white carbonate veins (Figs. 3A&B). The
203 brown to dark-gray carbonate veins are present as either part of a chaotic network of small veins
204 (<1 cm in thickness; Figs. 3A&B) or larger (up to 15 cm in thickness) veins preserved as pods
205 along the deformation bands dipping to the northwest at a medium to high angle (Figs. 3C&D).
206 Locally, these stretched carbonate veins are preserved at the contact zone between the high-strain
207 domain of the NSZ and the adjacent serpentinite and are parallelized to it. On fresh surfaces,
208 these veins range in color from milky white to grey or even dark gray. As described in Section 3,
209 the dark color of the deformation bands is related to the reaction-mediated formation of graphite
210 and the degree of transformation of carbonate to graphite varies from moderate (Figs. 3C&D) to
211 almost complete (Figs. 3E&F). Along these bands, zones in which carbonate transformation is
212 complete are marked by a complete absence of carbonate and the presence of graphite in
213 association with diopside. These deformation bands have been reworked multiple times during
214 the tectonometamorphic evolution of the NSZ, and some of the late-stage veins crosscut the
215 bands (Figs. 3C&D), whereas others are parallelized-to and transposed into it with a sinistral
216 (viewed top down) sense of movement (Figs. 3E&F).
217 The larger brown to dark gray carbonate veins are coarse-grained (grains up to 1-2 cm in
218 diameter) whereas the ones that are smaller have grains ranging from <1 mm to 0.5 cm in
219 diameter. All identified carbonate veins/pods contain at least some dark, graphite-bearing
220 domains. These carbonate pods appear brecciated, with graphite occupying the spaces between

221 breccia fragments, and also display evidence of ductile deformation with grain size reduction
222 (Figs. 3C, D, G&H). Smaller veins are generally darker and more reworked by ductile
223 deformation compared to larger carbonate pods. The samples selected for this study were
224 collected from these carbonate veins and pods and their microstructural and petrographic features
225 are presented in Section 3.
226
227 **2. METHODS**
228 **2.1 Petrographic investigations and MicroRaman analysis**
229 Petrographic and microstructural analyses were conducted using a Zeiss correlative
230 microscopy platform composed of an AxioZoom V16 macroscope, an AxioScope7 polarized
231 microscope, and a Zeiss EVO 15 Scanning Electron Microscope (SEM) at the Deep Carbon Lab
232 (https://deepcarbonlab.org), Department of Biological, Geological and Environmental Sciences,
233 University of Bologna, Italy. Detailed methodology for SEM-EDS-EBSD is presented in section
234 2.2.
235 Cathodoluminescence (CL) analyses were conducted using a Cathodyne optical CL setup
236 manufactured by NewTec Scientific, operated at 100 mTorr vacuum, an accelerating voltage of
237 12 kV and 100 mA current. CL intensity maps have been presented in Figs. 4C&E, in which
238 brighter shades of red correspond to increasing luminescence (black: least luminescence, orange:
239 maximum luminescence).
240 Raman spectra were acquired using a WITec Alpha 300-R confocal micro-Raman
241 spectrometer with a 532 nm laser source at the Department of Biological, Geological and
242 Environmental Sciences, University of Bologna, Italy. The Raman spectra were acquired with a
243 100x objective using the following parameters: 600 and 1200 g/mm grating; an on-sample laser

power between 25-40 mW and acquisition times ranging between 1-10 minutes. The Raman shift was calibrated using an Ar-Hg lamp. The acquired spectra of serpentine were compared with the data reported in (Schwartz et al., 2013) and Compagnoni et al. (2021) for serpentine minerals, and with the rruff.com database for carbonate minerals. The Raman spectra of fluid species were compared with those reported in Frezzotti et al. (2012). We performed quantitative Raman spectroscopy analysis to estimate the composition of the fluid species hosted in the FIs using the methods outlined in Burke (2001).

2.2 SEM-EDS-EBSD

EDS maps of regions of interest (ROI) within the samples studied were obtained using the Oxford Instruments Ultim max 100 silicon drift detector fitted to the Zeiss EVO 15 SEM at the Deep Carbon Lab, in high-vacuum mode. Samples were polished on a Saphir Vibromat with Eposal F (0.06 μm) for 4 hours followed by further polishing with Eposal M (0.01 μm) colloidal silica solutions. EDS data were obtained and subsequently processed using the TruMap background removal post-processing routine in the Aztec software suite (version 5.1), manufactured by Oxford Instruments. EBSD data were acquired from ROIs within the studied samples using an Oxford Instruments C-Nano EBSD detector fitted to the Zeiss EVO 15 SEM at the Deep Carbon Lab, operating in low-vacuum mode with a chamber pressure of 40 Pa. Data acquisition was carried out using the Aztec software suite (version 5.1) manufactured by Oxford Instruments, using an accelerating voltage of 25 kV, step sizes of 1 and 1.5 μm depending on the area of the ROI, a beam current of 8-10 nA, a sample tilt of 70º and working distances between 16-22 mm. In domains containing both calcite and dolomite, the TruPhase acquisition routine was utilized to accurately distinguish the two phases using EDS spectra at each analyzed point (Helpa et al., 2014), in addition to acquired diffraction patterns, owing to the substantial

crystallographic similarity between the 2 phases (calcite trigonal-high, Laue group -3m; dolomite trigonal low, Laue group -3). The magnesian calcite match unit was used to index dolomite in domains without calcite (trigonal-high, Laue group -3m). Raw indexing rates varied from 80-94%. The acquired EBSD data were processed using Aztec Crystal (version 3.1). A cleanup routine was used involving removal of wild spikes followed by 3 iterations of zero solution and removal by assigning unindexed pixels the average orientation of 3 nearest neighbors. Voids detected based on band contrast were excluded from the cleanup routine. Dolomite is prone to misindexing (Pearce et al., 2013) about the axis/angle pair that defines its growth twins (11-20 and 180º). Pseudosymmetry arising from this misindexing was removed by rotating misindexed portions up to 10 pixels wide into the orientation of the host grain. Post pseudosymmetry removal, the data was denoised using a Kuwahara filter constituted by octants of radii of 3 pixels. The processed and denoised data obtained from Aztec Crystal was used as the input file for Mtex 5.10.2 (Bachmann et al., 2010), which was used to plot interphase misorientations between dolomite and calcite based on the workflow presented in Morales (2022) and Zertani et al. (2024). Determination of the presence of a crystallographic preferred orientation (CPO) was done by plotting upper hemisphere equal area pole figures using a halfwidth of 10º using one pixel per grain to ensure that larger grains are not overrepresented. Poles to (0001), and (2-1-10) were plotted to determine the distributions of c and a axes, respectively while poles to (10-14), (01-12) and (01-18) were plotted to understand the prevalence of twinning in the microstructure. Grain reference orientation deviation (GROD) maps, that plot the pixelwise orientation deviation from the mean orientation of each grain, have been presented in Figs. 9-11 to visualize the internal substructures of dolomite and calcite grains from different textural domains. Low-angle (2º-10º) and high-angle (>10º) boundaries along with f-twins (misoriented 78º about 2-201) and

290 growth twins (misoriented 180º about 11-20) in dolomite and e-twins for calcite (misoriented 78º
291 about 20-21) were superposed onto the GROD maps. Disorientation (minimum misorientation)
292 angle distributions between neighbor pairs of grains (grains that share a common boundary;
293 shown in blue) and random pairs of grains (randomly chosen data points not related to grains
294 across a common boundary; shown in yellow) for dolomite and calcite have also been shown in
295 Figs. 9-11. The theoretical distribution of misorientations for a completely random fabric
296 (Mackenzie plot) is shown with a grey line in these figures. The M-index (Skemer et al., 2005), a
297 measure of the fabric strength (values between 0 and 1; 0 corresponds to a completely random
298 fabric and 1 corresponds to a fabric with a uniform orientation), has been calculated for each
299 textural domain and the value has been incorporated within the disorientation plots.

300 **2.3 Thermodynamic modelling**

301 To model the mineralogical evolution of carbonates under the infiltration of H_2-rich
302 fluid, pseudosections were computed with the Perple_X software packages (Connolly, 2005)
303 Two pseudosections were computed at 1 GPa and 2 GPa with temperature ranging from 300 °C
304 to 800 °C as y-axis and moles of H_2 added to the initial composition as the x-axis (see Section
305 3.4 for details on the considered pressure-temperature conditions). The initial composition was
306 set to that of a slightly ferroan dolomite with a Mg# of 5%, Mg# = Mg/(Mg+Fe). The x-axis
307 represents the evolution from 0 moles of H_2 added to the Fe-dolomite up to 5 moles of H_2 added.
308 The Holland and Powell (2011) version 633 thermodynamic database was used. The
309 pseudosections were computed in the CaO-MgO-FeO-C-H_2-O_2 system of components. No
310 excess O_2 was added to the initial dolomite composition. The solid solutions used were:
311 oCcM(EF) for Fe-Mg-Ca-carbonates (Franzolin et al., 2011), B for Fe-Mg-brucite (ideal
312 molecular mixing), Fper(H) for Fe-Mg-periclase (Holland et al., 2013), MF for Fe-Mg-magnetite

313 (Sack and Ghiorso, 1991) and COH-Fluid for H_2-CH_4-H_2O-CO-CO_2 fluid. Mineral abbreviations
314 were adopted from Holland and Powell (2011).
315
316 **3. RESULTS**
317 **3.1 Petrography**
318 Four samples from different parts of the NSZ (COR18-7a, COR18-7b, 3COR19-20Zb,
319 and 3COR19-20Zc, see Figs. 3C&G for thin-section locations), representing carbonate veins and
320 pods and the foliated serpentinite within which they are hosted, were chosen for this study. The
321 veins and pods contain variable proportions of dolomite, calcite, and serpentine as major mineral
322 phases, as well as minor chlorite, magnetite, sulfides, and apatite. COR18-7b is a sample of the
323 host serpentinite (Fig. 4A), COR18-7a (Figs. 4B&C) of a brecciated carbonate hosted along one
324 of the carbonate-bearing deformation bands developed along the NSZ and 3COR19-20Zb (Fig.
325 4D&E) and 3COR19-20Zc (Fig. 4F) are samples from the interface between carbonate veins and
326 serpentinite.
327 The host serpentinite (sample COR18-7b; Fig. 4A) contains a foliation defined by
328 elongated antigorite and minor chlorite and is cut by later concordant and discordant veins of
329 chrysotile that will not be described further. Several kink bands deform the serpentine grains at
330 right angles to the foliation (Fig. 5A). The host serpentinite underwent a phase of brittle
331 deformation post-dating the development of its pervasive regional foliation, as evidenced by the
332 presence of graphite-filled fractures cutting across the foliation. This phase of deformation
333 involved the formation of fractures at high angle to the serpentinite foliation and the subsequent
334 widening of these fractures and their infilling by carbonate (Fig. 4A).

A carbonate pod hosted within one of the deformation bands within the NSZ (COR18-7a; Figs. 4B&C) consists of, in order of abundance, dolomite, calcite, serpentine (mostly antigorite), and graphite, with minor magnetite as an accessory phase (Fig. 4B). Dolomite and calcite were distinguished based on CL and EDS maps (Figs. 4C&E and Fig. 7). In the CL maps, dolomite appears darker, and calcite appears brighter (Figs. 4C&E). The microstructures of dolomite vary from domains consisting of brecciated coarse-grained dolomite to high-strain domains composed of aggregates of fine-grained dolomite formed by fracturing of the coarser grains, with transitional domains between the two endmembers (Figs. 4B&C). In the brecciated domains of the sample, individual grains are up to 1 mm wide, with an average width of 500 microns. They contain a high density of twins, show no evidence of substantial recrystallization, and exhibit nearly perfect extinction patterns in the untwinned domains (Fig 4B, 5B). The brecciated fragments have angular shapes, with straight to curvilinear boundaries (Fig. 5B). Curved segments of the boundaries between the brecciated fragments have a serrated appearance, resembling stylolites, and attest to the occurrence of dissolution-precipitation at the margins of the breccia fragments.

The deformed interface between a carbonate vein and the host serpentinite within the NSZ is presented in Figs. 3G&H and exhibits a layered structure defined by a stack of a carbonate-dominated layer (sample 3COR19-20Z), a layer of carbonate + serpentinite clasts and a layer of sheared diopside in contact with the serpentinite. Graphite is present in all layers. The diopside + graphite layer is interpreted to be indicative of complete reaction between carbonate and serpentine in the presence of H_2 (Vitale Brovarone et al., 2017). We focused on slab 3COR19-20Z because it records an incipient (i.e., not complete) stage of fluid-carbonate interaction. This sample shows a continuum of microstructures from brittle (3COR19-20Zb) to

ductile (3COR19-20Zc; Figs. 3G&H, 4D-F). Within the carbonate-dominated layer, a domain of brittle microstructures similar to those observed in COR18-7a and characterized by angular fragments of twinned dolomite grains lined by graphite, transitions into domains consisting of aggregates of dolomite characterized by substantial grain size reduction (Figs. 4D-F). Within the fine-grained domains, larger relict grains of dolomite are surrounded by small subgrains, resembling core-mantle textures (Fig. 5C). The size of the dolomite grains decreases from 1 mm in the brecciated domains to 100-200 microns in the fine-grained domains. There is also a variation in grain shapes of the fine-grained dolomite compared to the brecciated dolomite. The fine-grained dolomite grains transition to more rounded shapes from elongate grains and are observed to show a depletion in their Fe contents from core to rim (Fig. 6B). Boundaries between the finer grains are rarely straight, whereas the brecciated dolomite grains are mostly equant with well-defined grain boundaries that occasionally deviate from linearity owing to the development of stylolites at the interfaces between grains. While some of the larger fragments contain abundant twin boundaries, the smaller grains are completely devoid of them (Figs. 5E&6C).

Within the domains dominated by brecciated dolomite (3COR19-20Za and b and COR18-7a), calcite occurs in close association with the dolomite (Figs. 5F, 6 A&C, 7E-H). In the brecciated domains, calcite proportions are low, with incipient calcite formation observed along the boundaries of the dolomite grains, especially at junctions among dolomite fragments (Fig. 5F, 6A). Away from the brecciated domains in COR18-7a and 3COR19-20Zb, calcite occurs in wider domains up to tens of microns thick, closely associated with graphite and magnetite. In these domains, the calcite grains are euhedral to subhedral and rounded (Figs. 5G, 6D, 7 I-L). The proportion of graphite and magnetite correlates well with the amount of calcite present, with relatively higher graphite proportions in the wider calcite-dominated domains

compared to the domains of incipient calcite formation associated with the brecciated dolomite grains. Nonetheless, within the brecciated domains, zones with relatively higher calcite proportions also contain abundant graphite along fractures and twin boundaries within dolomite (Fig. 5F, 6C).

The domain of fine-grained dolomite is characterized by drastic grain-size reduction and passes laterally in a domain composed of diopside and graphite along with pervasive discordant calcite veins (3COR19-20Zc, Fig. 5H). The diopside grains are fine-grained (average grain diameter of 50 microns), with individual grains not exceeding 100 microns in diameter, and are rounded and anhedral. They are localized into an extensively sheared domain dissected by conjugate sets of fractures. The entire unit is cross-cut by late-stage carbonate veins (Fig. 5H).

3.2 Fluid inclusion petrography and micro-Raman Spectroscopy

The dolomite grains within the brecciated domains have cloudy cores, owing to the occurrence of several fluid inclusions. These fluid inclusions are mostly biphasic containing liquid and vapor and are characterized by variable shapes, from irregular to negative crystal. They are mostly localized along trails that cross-cut twin boundaries. The size of the inclusions is variable, ranging from 5 microns in length to less than a micron. Some inclusions are notably monophasic, consisting of a singular vapor phase (Fig. 8A). Raman spectra obtained from monophasic fluid inclusions within the brecciated dolomite grains (Fig. 8B) confirm the presence of CH_4, characterized by a Raman shift ranging between 2913 cm^{-1} and 2916 cm^{-1}, as the dominant vapor phase with subordinate amounts of H_2, displaying a Raman shift at 4153 cm^{-1}. Fluid inclusions in the relict dolomite grains from the fine-grained high-strain domains (Fig. 8C) are also characterized by their abundance and negative crystal shapes, as in the brecciated

dolomite domains but the proportion of monophasic vapor-only inclusions is substantially higher and biphasic liquid + vapor inclusions are rare. The Raman spectra of fluid inclusions within the relict dolomite grains from the high-strain domain confirm the presence of H_2 as the dominant fluid component featuring Q1 vibrational bands at 4127, 4144, 4156 and 4162 cm^{-1} and the S0 (1) rotational band at 585 cm^{-1} (Fig. 8D). Fluid inclusions within calcite are much less abundant compared to the brecciated and relict dolomite grains. When present, they are localized adjacent to grain boundaries and occur within transgranular trails (Fig. 8E). The fluid inclusions within calcite are commonly monophasic with negative crystal shapes and biphasic inclusions are very rare, similarly to the fluid inclusions in the relict dolomite grains from the high strain domains. The inclusions in calcite also show a greater variability in size, ranging from up to 15 microns in length to less than a micron (Fig. 8E). Calcite-hosted fluid inclusions (Fig. 8F) consist of a vapor phase dominated by CH_4 (2912 cm^{-1}) with subordinate amounts of H_2 (4149 cm^{-1}).

Fluid inclusions were also studied in a sample from a large diopside vein hosted in serpentinite from the hanging wall of the NSZ to ascertain whether the H_2 hosted in the fluid inclusions within carbonate of the NSZ was externally or internally derived, since this diopside vein is located at the edge of the NSZ, more than 200 m from the carbonate-rich deformation bands within the NSZ. The vein is concordant to the regional foliation of the serpentinite and is composed of large (> 1 cm) diopside crystals elongated parallel to the main lineation in the antigorite serpentinite. This feature indicates that diopside formed or at least recrystallized during the metamorphic evolution of the unit. Diopside contains large, biphasic liquid + vapor fluid inclusions. These inclusions are rich in CH_4 and H_2 (Fig. 8G&H). We undertook quantitative estimates of the proportion of CH_4 and H_2 in the vapor phase in 5 carbonate-hosted fluid inclusions and one diopside-hosted fluid inclusion from within the NSZ. Four out of five

carbonate hosted fluid inclusions contain a higher molar proportion of CH_4 compared to H_2; in contrast, the diopside-hosted fluid inclusion contains higher proportion of H_2 relative to CH_4 (Table 1).

Raman spectra were also used for the identification of antigorite as the dominant serpentine species (Supplementary figure S1B) and to confirm the presence of graphite (Supplementary figure S1D).

3.3 EBSD analyses

EBSD data were acquired from the three texturally distinct domains that were recognized in these samples. These domains consist of (1) high-strain domains composed exclusively of fine-grained dolomite (domain 1; Figs. 5C&9A), (2) brecciated dolomite with incipient development of calcite at the margins of breccia fragments (domain 2; Figs. 5E, 6C&10A), and (3) domains of advanced calcite formation (domain 3; Figs. 5G&11A).

In the high-strain domains (domain 1; Fig. 9), dolomite appears to preserve core-mantle textures. The GROD map (Fig. 9A) from this domain shows that larger relict grains of dolomite have much higher GROD values compared to the finer grains that surround it (up to 15º in the relict grain). The proportion of low-angle boundaries is also higher in the relict grains compared to the grains in the matrix (Fig. 9A). These observations appear to suggest that the dolomite grains in this domain underwent subgrain rotation (SGR) recrystallization, wherein original subgrains within larger grains of dolomite progressively rotated into new orientations (Lloyd et al., 1997; Bestmann and Prior, 2003; Passchier and Trouw, 2005). However, both the cumulative misorientation (misorientation at a point relative to the misorientation at the first point; shown in red) and the point-to-point misorientation (misorientation at each point of the profile; shown in blue) curves (Fig. 9B) along the white line through the center of the relict grain in Fig. 9A show

sharp peaks and troughs, typical of healed microcracks (Schenk and Urai, 2005; Anders et al., 2014; Hentschel et al., 2019) and do not correlate with a gradual increase in misorientation as would be expected for SGR recrystallization (Bestmann and Prior, 2003; Passchier and Trouw, 2005; Lopez-Sanchez et al., 2021). Therefore, the finer grainsize fraction of dolomite probably originated due to fracturing of coarser dolomite grains, and not by the formation and rotation of subgrains in coarse-grained dolomite into new orientations.

In the domains of incipient calcite formation (domain 2; Fig. 10A), the larger relict grains of dolomite are dominated by twin boundaries, while the smaller dolomite grains within the matrix are free of twin boundaries. Both f-twins and growth twins are observed within dolomite. The relict, twinned grains of dolomite show higher GROD values (~7º) compared to the smaller dolomite grains surrounding it. In this case, the proportions of low-angle boundaries in both the relict, coarser grains of dolomite as well as the finer-grained dolomite within the matrix are low, reinforcing a fracture-based origin for the finer grainsize fraction of dolomite instead of SGR recrystallization. In the domains of advanced calcite formation (domain 3), recrystallized dolomite grains are absent, but larger relict grains of dolomite with growth and f-twins persist (Fig. 11A). In this domain, the distribution of GROD values is broadly consistent with that observed in the domain of incipient calcite formation. A higher GROD value is observed within the relict and twinned dolomite grain (~6º), whereas GROD values in the adjacent calcite-rich matrix is generally low (between 0º-6º) except for intermediate values in some larger grains.

Within the high-strain domain (domain 1), dolomite shows a substantial spread in both neighbor pair and random pair misorientations (Fig. 9C). The lack of a discernible CPO is reflected in the pole figure plots (Fig. 9D) in which the <c> axes of dolomite are concentrated into a broad girdle of orientations sub-parallel to the main shear plane of the NSZ and there are no CPOs observed

for the <a> axes [2-1-10], rhomb planes (10-14) or f planes (01-12). The absence of a strong CPO is also reflected in the very low M-index value for the fabric in this domain (0.082; Fig. 9C).

In the domains of incipient calcite formation (domain 2; Fig. 10), random pair misorientation distributions of dolomite show a wide spread in values, while neighbor pair misorientation distributions show strong peaks at misorientations corresponding to f-twin (78º) and growth twin (180º) boundaries (Fig. 10B). The spread in neighbor pair misorientation distributions is manifested as an intermediate M-index value of 0.202 for the dolomite fabric. The twin-dominated CPO of dolomite is reflected in the pole figures as well (Fig. 10D). The basal planes of the dolomite grains in this domain are strongly aligned sub-parallel to the foliation, as evidenced by the strong concentration of poles to (0001) at almost right angles to the mesoscopic foliation and near-alignment of the <a> axis along the foliation. The CPOs of the f-planes (01-12) of the dolomite grains are characteristic of f-twinning, with 2 sets of orientation clusters in close proximity and one set of overlapping orientations. The misorientation distribution of calcite, on the other hand, is substantially different compared to that of dolomite, with strong random pair misorientation peaks between 20º-100º (Fig. 10C) while the neighbor pair misorientation distribution shows a wider spread in orientations. The strong peaks of random pair misorientations are reflected in a strong M-index value of 0.764 for the calcite fabric in this domain. The <c> axis distributions of calcite (Fig. 10D) show a strong preferred orientation at a high angle to the mesoscopic fabric. There is one set of overlapping <c> axis orientations between calcite and dolomite (highlighted with a red circle in Fig. 10D) suggesting an inheritance of orientations from dolomite to calcite. No CPOs are observed for the <a> axes, rhomb or e-planes of calcite grains in this domain. Interphase misorientations between calcite

and dolomite were plotted to investigate the crystallographic relationships between calcite and dolomite in the domains of incipient and advanced calcite formation (Figs. 10E&11E). In the domains of incipient calcite formation, 37.59% of the boundaries between calcite and dolomite are low-angle boundaries (Fig. 10E), suggesting growth of calcite on dolomite by fluid-mediated interface-coupled dissolution-precipitation rather than deposition from a Ca^{2+}-rich fluid (Putnis et al., 2005; Ruiz-Agudo et al., 2014; Spruzeniece et al., 2017; Moore et al., 2024).

In domains where calcite formation is more advanced (domain 3; Fig. 11), calcite grains form layers up to 1 mm wide and are texturally different compared to the domains of incipient calcite development. There is a contrast in fabric strength (Figs. 11B&C) as well, with dolomite characterized by a strong fabric (M-index 0.9) compared to a weak fabric for calcite (M-index 0.11), although the high M-index of dolomite in this domain is strongly influenced by the presence of a single, large, twinned grain of dolomite. There is no observable CPO for the calcite grains in this domain (Fig. 11D) and the mean grain size of calcite is quite small (25.47 μm). The relatively small grain size in conjunction with the absence of a strong CPO leads us to conclude that calcite grains in this domain deformed primarily by diffusion creep accommodated by grain boundary sliding. The substantially lower proportion of low angle boundaries between calcite and dolomite in this domain (6.21%, Fig. 11E) can be attributed to the onset of diffusion creep in calcite, wherein initial low-angle boundaries were subsequently modified by grain rotation to high angle configurations.

To summarize the results of our EBSD-based textural analyses, strain accommodation within the carbonates of the NSZ was initially restricted to twinning in coarse grained dolomite, followed by fracturing and comminution of the twinned dolomite grains. Fracturing of the twinned dolomite resulted in the formation of fine-grained aggregates of dolomite (domain 1)

519 that were subsequently reorganized into high-strain zones, as well as the development of a
520 fracture network that created high permeability pathways for subsequent ingress of H_2. Although
521 the relatively higher proportion of low-angle boundaries in the relict dolomite grains from the
522 high strain domain may suggest an origin of the fine-grained dolomite aggregate by SGR
523 recrystallization, we do not observe a similar distribution of low angle boundaries in coarser
524 dolomite grains from domain 2 and 3 that contain abundant growth and f-twins. Additionally,
525 misorientation profiles constructed across relict dolomite grains in domain 1 (Fig. 9B) show
526 sharp peaks in misorientation which are more commonly indicative of healed microcracks rather
527 than the pervasive operation of SGR recrystallization. This further suggests a fracture-based
528 origin for the fine-grained dolomite aggregates observed in domain 1.

529 While Raman spectra of fluid inclusions (Section 3.2) confirm the presence of H_2 in all
530 the microstructural domains described previously, the products of carbonate reduction are
531 variable. Within the high strain domains (domain 1), calcite is noticeably absent with dolomite
532 being associated with graphite and magnetite, whereas in the other microstructural domains,
533 calcite is present as a product of interface-coupled dissolution of dolomite (domain 2), or as fine-
534 grained aggregates in high-strain zones around dolomite (domain 3), in association with graphite
535 and magnetite. Therefore, graphite and magnetite are interpreted to have formed at multiple
536 stages across the dolomite-calcite transformation, and thermodynamic models presented in the
537 next section have been developed to explain these observations.

538

539 **3.4 Thermodynamic modelling**

540 The microstructurally constrained chronology of carbonate transformation in the studied
541 samples indicates a progressive transition from Fe-bearing dolomite to Fe-poor dolomite and

542 finally to Ca-carbonate (calcite). Graphite and magnetite are found in microstructural association
543 with Fe-poor dolomite in the high-strain domains and with calcite in domains where carbonate
544 transformation has proceeded to completion.

545 In order to constrain the conditions of dolomite transformation and the role of reducing
546 fluids like H_2 and CH_4 in facilitating this transformation, we calculated thermodynamic models
547 of H_2-dolomite interactions at 1 and 2 GPa, and in the 300 °-800 °C temperature range (Figs.
548 12&13). The two considered pressures represent the peak metamorphic pressure of the
549 Lawsonite eclogite-facies unit of Alpine Corsica (about 2 GPa; Vitale Brovarone et al., 2013),
550 and a retrograde pressure condition (1 GPa), consistent with the minimum temperature
551 conditions of the antigorite stability field (380-400 °C, Schwartz et al., 2013) according to the
552 tentative retrograde path suggested by Vitale Brovarone et al. (2011).

553 At 1 GPa and temperatures above ~460 °C, the addition of H_2 to dolomite results in the
554 formation of an assemblage consisting of dolomite + brucite + graphite. This might reflect the
555 observed chemical zonation in dolomite from the high strain domains in sample COR18-7a (Fig.
556 6B). Dolomite grains in this domain show progressive Fe depletion from core to rim but are not
557 associated with calcite. Increasing H_2 in the system is followed by the addition of calcite to this
558 assemblage with further addition of H_2 leading to the formation of magnetite (Fig. 12A). The
559 formation of magnetite is a consequence of the destabilization of the ferroan component of
560 dolomite after approximately adding 1.5 moles of H_2 to the system (Fig. 12B&C). At
561 temperatures below ~460 °C, the progressive addition of H_2 results in the formation of dolomite
562 + calcite + brucite + graphite, and subsequently magnetite. In this case, the thermodynamic
563 model predictions reflect the preserved assemblages in all the microstructural domains except the

564 dolomite-rich high-strain zones (domain 1), with calcite, graphite, and magnetite in intimate
565 microstructural association with dolomite (See Figs. 6A, C&D).

566 At 2 GPa and between 400-600 °C, dolomite + aragonite is converted to an assemblage
567 of dolomite + brucite + aragonite + graphite with magnetite being introduced into the assemblage
568 after the addition of ~1.5 moles of H_2 (Figs. 13A-D). The overall evolution is similar to that
569 computed for 1 GPa, with the only major difference being the existence of the Ca-carbonate-free
570 assemblage (dolomite + brucite + graphite) at higher temperature (above 600 °C). The formation
571 of magnetite in both cases requires the addition of ~1.5 moles of H_2 to the system. The absence
572 of brucite in the samples from the NSZ may be explained by the high solubility of Mg at the
573 pressure-temperature (PT) conditions encountered by the rocks of the NSZ (see Vitale Brovarone
574 et al., 2017 for a similar interpretation) or by the presence of silica in the natural samples, which
575 may have favored the formation of silicates such as serpentine or diopside.

576 **4. DISCUSSION**

577 Our study investigates the link between H_2 infiltration and the microstructural evolution
578 of carbonates in a subduction zone setting, as testified by field, petrological, and microstructural
579 data in conjunction with thermodynamic modelling results. Depending upon the amount and the
580 PT conditions of H_2 infiltration, we see substantial differences in microstructure and overall
581 rheology within the rocks of the NSZ. These differences and their controlling parameters are
582 discussed in the following sections.

583 **4.1 Origin and conditions of formation of molecular hydrogen, methane, and**
584 **graphite**

585 Despite the substantial microstructural heterogeneity observed at the scale of our study,
586 the ubiquitous circulation of H_2 in all stages of the microstructural evolution of these rocks is

587 evidenced by the presence of H_2 in fluid inclusions in dolomite from both the brecciated and
588 fine-grained domains, as well as in calcite from the domains of advanced calcite formation
589 (Section 3.2). The origin of the H_2 in these rocks can be attributed to three processes: (i) aqueous
590 alteration of Fe^{2+} to Fe^{3+} during serpentinization contemporaneous with subduction [see Vitale
591 Brovarone et al. (2020) for equivalents in Alpine Corsica], (ii) the release of H_2 from preexisting
592 serpentinites [see Malvoisin et al. (2012) for equivalents in Alpine Corsica], or (iii) aqueous
593 alteration of the siderite component of carbonate minerals (Milesi et al., 2015; Tao et al., 2018),
594 following the generic reaction:

595 $$3FeCO_3 + H_2O = Fe_3O_4 + 3CO_2 + H_2 \quad [1]$$

596 The first two processes would imply the infiltration of external, i.e., serpentinization- or
597 serpentinite-derived, H_2-rich fluids, whereas the third process would imply internally derived
598 fluids inside the carbonate pods. In our study area, we have documented the presence of H_2 in
599 fluid inclusions hosted within diopside veins in the serpentinite adjacent to the NSZ (see Table
600 1), in addition to the H_2-bearing inclusions in carbonates within the NSZ. In the diopside veins
601 adjacent to the NSZ, the molar fraction of H_2 relative to CH_4 is higher compared to carbonate-
602 hosted fluid inclusions within the NSZ, except for fluid inclusions within the brecciated
603 dolomite, which are gaseous and contain only H_2. The presence of H_2 outside the NSZ
604 carbonates and inside ultramafic rocks in their vicinity favors an external origin for the H_2 that is
605 responsible for the reduction of the studied carbonates. This feature suggests that at least a
606 fraction of the CH_4 observed in the carbonate pods formed through H_2-carbonate interactions
607 inside the pods. The presence of CH_4 in the diopside veins may be interpreted as a result of the
608 syn-serpentinization conversion of carbon-bearing species present in aqueous metamorphic
609 fluids to CH_4 during serpentinization (Vitale Brovarone et al., 2020; Boutier et al., 2021). The

610 presence of H_2 gaseous inclusions in the brecciated dolomite domains may testify to the incipient
611 infiltration of H_2 in response to fluid overpressure.

612 A subsequent phase of comparatively minor, in-situ H_2 production by aqueous alteration
613 of the siderite component of dolomite and self-reduction of dolomite to CH_4 is also suggested by
614 the presence of magnetite particles in reacted portions of the carbonate pods and the
615 microstructural relationships with calcite and graphite (Figs. 6 A-D). Our thermodynamic
616 modelling results indicate that the observed mineralogical evolution in the samples from the NSZ
617 can be explained by protracted infiltration of H_2-rich fluids at conditions either close to peak
618 metamorphic conditions (470-520 °C and 2-2.2 GPa, Vitale Brovarone et al., 2013), as well as
619 PT conditions experienced during retrograde cooling across ~460 °C and 1GPa (threshold
620 temperature for different reaction pathways as derived from thermodynamic modeling). The
621 presence of Ca-carbonate-free reacted domains suggests that, at least locally, the process started
622 at near peak metamorphic conditions (2 GPa), whereas the common presence of calcite in most
623 of the samples indicates that the process protracted (continuously or episodically) during
624 exhumation. The presence of antigorite in all the studied microstructures indicates that H_2
625 infiltration occurred at temperatures > 380-400 °C (Schwartz et al., 2013). It is possible to
626 estimate a maximum amount of H_2 infiltration using Figures 12 & 13. At 2 GPa and 500 ºC and
627 at 1 GPa and 400 °C, 2 moles of H_2 are necessary to fully react 2 moles of dolomites to form
628 graphite + Ca-carbonate + magnetite + brucite + fluid. At these pressure and temperature
629 conditions, the molar volume of dolomite is almost similar (32.34 and 32.65 cm^3/mol,
630 respectively), therefore the volume and mass of H_2 infiltrated are very similar. This implies that
631 full reaction of 1 cm^3 of dolomite requires the infiltration of 0.06 g of H_2 at the considered
632 conditions, and 60 kg H_2 are required to completely reduce a cubic meter of dolomite.

633 The presence of graphite in the rocks from the NSZ can be attributed to the saturation of
634 carbon in the fluid after reduction of carbonate minerals during H_2 infiltration. Firstly, this is
635 suggested by the microstructural association of graphite and carbonate, with graphite forming
636 along preferential fluid pathways, such as grain and phase boundaries and fractures in the
637 carbonate phases, especially dolomite (Figs. 5B, E, F&G and Figs. 6A-D). This is also suggested
638 by the thermodynamic modelling results presented in Section 3.4. This mechanism of graphite
639 precipitation is equivalent to the one described by Malvoisin et al. (2012) and Galvez et al.
640 (2013) along a blueschist-facies serpentinite-metasediment contact of Alpine Corsica, or to the
641 H_2-mediated reduction of carbonated serpentinites in the Lanzo massif, Western Italian Alps
642 (Vitale Brovarone et al., 2017; Giuntoli et al., 2020). The partial conversion of CH_4 to graphite
643 following carbon saturation in the fluid may also be responsible for at least a fraction of the CH_4
644 found in fluid inclusions, following the generic reaction:

645 $$CH_4 = C + 2H_2 \quad [2]$$

646 **4.2 Chronology of deformation and metamorphic events associated with H_2**
647 **infiltration and carbonate transformation along the Negru Shear Zone**

648 Based on our observations, we suggest, following the initial phase of dolomite
649 precipitation within the pods and veins of the NSZ, the resulting post-precipitation sequence of
650 chemical-mechanical events recorded by the carbonates within the studied samples:

651 1) An initial phase of deformation of dolomite above ~300 °C is suggested by the
652 abundance of twin boundaries in the brecciated fragments of dolomite. The development of f-
653 twins is the principal mode of strain accommodation in dolomite at temperatures ranging from
654 300º-600 ºC (Barber and Wenk 1979; Barber et al. 1981) and the substantial proportion of f-
655 twins in the brecciated fragments of dolomite constrain the first phase of deformation to

656 temperatures in the aforementioned range. A temperature > 380-400 °C is also suggested by the
657 presence of antigorite (Schwartz et al., 2013). The preservation of antigorite without any
658 evidence of dehydration, in association with the carbonates, additionally constrains temperature
659 of deformation to less than 600 °C (Perrillat et al. 2005).
660 2) Subsequently, the twinned dolomite underwent a phase of brecciation forming a
661 fine-grained dolomite aggregate, which initiates a switch from a brittle to a semi-brittle
662 deformation regime (Gratier et al., 1999; Trepmann and Stöckhert, 2003; Fusseis and Handy,
663 2008; Menegon et al., 2013; Reber and Pec, 2018). Although the high-strain domains appear to
664 preserve possible textural evidence of SGR recrystallization (see Section 3.3, Fig. 9) in the form
665 of low-angle boundaries in relict dolomite grains, the low-angle boundaries within these relicts
666 do not define polygonal subgrains, are associated with sharp changes in misorientation (Fig. 9B)
667 and may well represent undulatory extinction/lattice distortions and/or healed microcracks and it
668 is plausible that the smaller grains within the high-strain domains originated as fragments
669 derived from fracturing of the coarser grains of dolomite. As highlighted previously, the
670 persistence of antigorite and the presence of twins in dolomite coupled with previous
671 temperature constraints (430-470 ºC) obtained using Raman spectroscopy of carbonaceous
672 material on metasedimentary lithologies from the same lawsonite-eclogite unit (Vitale Brovarone
673 et al. 2013) constrain deformation temperatures to a range not suitable for the operation of
674 dynamic recrystallization of dolomite (Higgs and Handin 1959; Barber et al. 1994; Newman and
675 Mitra 1994; Delle Piane et al. 2009; Holyoke et al. 2013, 2014; Berger et al. 2016; Li et al.
676 2021). In detail, dolomite deforms by climb-assisted deformation above 600 °C (Barber et al.,
677 1981), whereas twinning is the dominant mode of strain accommodation between 300-600 °C
678 (Newman and Mitra, 1994). Fine-grained high-strain domains can originate in two ways: 1) they

679 may form as a result of fluid-induced dynamic recrystallization (Newman and Mitra, 1994;
680 Rutter and Brodie, 1995; Pennacchioni and Mancktelow, 2007; Fusseis and Handy, 2008;
681 Goncalves et al., 2016) or, alternatively, 2) an initial phase of entirely brittle deformation can
682 lead to the formation of a finer-grained matrix in which strain can subsequently localize (Imon et
683 al. 2004; Brander et al. 2012; Menegon et al. 2013; Moore et al. 2024). Based on temperature
684 constraints obtained from the thermodynamic modelling presented in Section 3.4 coupled with
685 our textural observations presented in Section 3.3, we attribute the grain size reduction of
686 dolomite to fluid-induced fracturing, which led to the subsequent development of the high strain
687 domains within the fine-grained dolomite layers. The relict dolomite grains in the high strain
688 zones contain H_2-bearing fluid inclusions which points to the initial brecciation of the dolomite
689 being induced by fluids containing H_2, although the absence of calcite suggests that proportions
690 of H_2 within the fluid must have been low, at least initially (less than 2 moles of added H_2; see
691 Fig. 12). Once a pronounced grain size contrast was established between the coarse-grained
692 brecciated dolomite and finer-grained dolomite within the high strain domains, a strength
693 contrast was established such that subsequent deformation localized within the weaker fine-
694 grained shear zones, whereas the stronger angular breccia fragments deformed locally by twin
695 gliding and minor crystal plasticity. These observations correlate well with previous studies on
696 natural examples of fine-grained dolomite shear zones (Newman and Mitra, 1994), in which the
697 effect of grain size variations in the localization of strain in dolomite aggregates was established.
698 Additionally, continuous viscous deformation of the fine-grained dolomite grains around the
699 rigid lenses of the coarse-grained brecciated dolomite leads to the build-up of stresses, eventually
700 triggering brittle failure of these lenses (Fagereng and Diener 2014). The newly formed

transgranular fractures in the twinned dolomite fragments increased the secondary porosity, leading to later and renewed infiltration of H_2-rich fluids.

3) Based on our thermodynamic modelling of Section 3.4, the latter stages of H_2 infiltration led to the reduction of dolomite to calcite + graphite + magnetite, with the proportion of calcite directly linked to the amount of H_2 infiltration. A distinction is made between the different phases of H_2 infiltration based on the presence of calcite + graphite + magnetite. This assemblage is noticeably absent in the high-strain domains but is ubiquitous around the margins of brecciated dolomite and along the tips of transgranular fractures within twinned dolomite fragments. Our modelling results indicate that the assemblage of calcite + graphite + magnetite can be derived from dolomite in the presence of H_2-rich fluids at temperatures between 300-600 °C at 2GPa (near peak metamorphic conditions) or close to 460 °C at 1GPa (retrograde path). At these temperatures, deformation of dolomite is limited to twin gliding and minor crystal plasticity accommodated by low angle boundaries without substantial dislocation motion (Higgs and Handin 1959; Barber and Wenk 1979; Barber et al. 1981, 1994; Newman and Mitra 1994; Delle Piane et al. 2009; Holyoke et al. 2013, 2014; Berger et al. 2016; Li et al. 2021). On the other hand, calcite is rheologically weaker compared to dolomite at those temperatures (Viola et al. 2006; Delle Piane et al. 2009; Kushnir et al. 2015), and based on our microstructural observations from the domains of advanced calcite formation, we can conclude that infiltration of H_2-rich fluids at temperatures ~460 ºC and 1GPa led to the formation of a layer of fine-grained calcite into which strain was localized by a combination of grain boundary sliding and diffusion creep (see Section 3.3 and Fig. 14 for a summary).

Based on our results, we can identify two alternative mechanisms by which H_2 infiltration can influence the deformation of carbonate-rich lithologies. The first mechanism involves fluid

overpressure at temperatures above 460 °C and P of ~1GPa, which leads to an initial phase of brecciation of dolomite and formation of a fine-grained aggregate wherein subsequent strain is localized, forming shear zones. The second mechanism involves deformation at conditions at which calcite stability is enhanced in the presence of H_2 (see Section 3.4), leading to a phase transition from dolomite to calcite and resulting in substantial rheological weakening due to viscous flow of calcite at these pressure and temperature conditions. Both brittle and ductile phases of deformation within the NSZ can be attributed to the infiltration of H_2-rich fluids, but at different stages and PT conditions. This also explains the variability in calcite occurrence in different domains as the proportion of calcite formed from dolomite is dependent on the efficiency of hydrogen ingress.

Thus, the rocks collected in close association with the NSZ constitute a unique instance of deformation induced by infiltration of H_2-rich fluids and provides insights into the mechanisms by which H_2 can circulate along a subduction interface shear zone.

4.3 Mechanical effects of H_2 infiltration

The effect of H_2 infiltration into crustal rocks is relatively unknown barring a couple of recent studies (Giuntoli et al., 2020, 2024) whereas the effect of infiltrating H_2 as a facilitator for embrittlement processes such as stress corrosion cracking of metals has been known for some time (Su et al., 1992; Scully et al., 2012; Robertson et al., 2015; Braid et al., 2024). While brittle creep of geological materials linked to stress corrosion induced by H_2O is well known (Anderson and Grew, 1977; Michalske and Freiman, 1982; Atkinson, 1984; Brantut et al., 2013), there currently exists a knowledge gap between laboratory results of H_2 embrittlement and corrosion cracking and their potential manifestation in natural environments such as natural H_2-rock reactions or underground hydrogen storage (UHS) in geologic reservoirs. Although this study

747 could not provide evidence for direct analogues of the typical microstructures of H_2
748 embrittlement and corrosion cracking as observed in material science experiments, our results
749 provide an opportunity to assess the potential contribution of these processes in a geologic
750 environment. The brecciated dolomite grains within the NSZ probably underwent multiple
751 phases of brittle deformation, as evidenced by multiple generations of transgranular and
752 intragranular fractures of varying orientations (see Section 3.1). While some of the fracture
753 generations might be related to stress buildups along rigid lenses of carbonate and others to fluid
754 overpressure, the morphologies of some intragranular fractures appear well-correlated with those
755 formed due to H_2-induced stress corrosion cracking (Woodtli and Kieselbach, 2000). Within the
756 domains of incipient calcite formation, we observe calcite nucleation at the boundaries between
757 fragments, where they are intersected by transgranular fracture tips (Figs. 5F, 6A). A key
758 criterion for the identification of stress corrosion cracking is the localization of reactions at the
759 leading edge of fracture tips, instead of alteration along the entire length of the fracture owing to
760 enhanced access of reactants (Anderson and Grew, 1977; Barnett and Kerrich, 1980; Brantut et
761 al., 2013), which correlates well with our observations of incipient calcite nucleation at the
762 margins of the dolomite breccia fragments. The net effect of the stress corrosion cracking of
763 dolomite and subsequent formation of calcite is a positive volume change of 16% owing to the
764 volume change resulting from the conversion of one molecule of dolomite to two molecules of
765 calcite (Michałowski and Asuero 2012). This volume increase accompanying the transformation
766 of dolomite to calcite may lead to the development of a positive feedback loop as progress of the
767 reaction leads to the formation of newer fractures that enhance permeability (Yoshida et al.,
768 2020; Renard, 2021).

769 **5. CONCLUSIONS**

The rocks of the NSZ constitute a unique natural laboratory to study deep H_2 migration in the crust and the chemical-mechanical effects of H_2 ingress within crustal carbonates. The carbonates of the NSZ preserve a continuum of microstructures attesting to deformation occurring in both the brittle and ductile regimes, with a pronounced role of H_2-rich fluids as a common influence across all stages. An initial phase of brittle deformation of dolomite occurred due to overpressure developed by the accumulation of H_2-rich fluids formed by serpentinization occurring in the vicinity of the NSZ. The brittle fracturing of the dolomite grains had two important implications:

1) The formation of a finer-grained matrix that weakened the rock and localized subsequent strain.

2) Formation of high permeability pathways that facilitated the infiltration of H_2 which led to the formation of calcite+graphite+magnetite. In addition to brittle deformation due to fluid overpressure, at least one phase of intra and intergranular fractures in dolomite have morphologies typical of those produced by H_2-induced stress corrosion cracking. These mechanisms are well established in material sciences, but still not documented in natural rocks.

Transformation of dolomite to calcite during exhumation appears to be directly correlated with the amount of infiltrating H_2 and varies even on the scale of a single thin-section, with different identifiable textural domains ranging from domains of incipient calcite formation to domains of advanced calcite formation. Our thermodynamic results indicate that full reaction of 1 m^3 dolomite required the infiltration of ~60 kg of H_2, and these calculations provide a first-order estimate of paleo-H_2 fluxes in subducted lithosphere. A strong rheological contrast is established in the domains of advanced calcite formation owing to the pronounced difference in strength between calcite and dolomite. The coarse dolomite grains in this domain preserve

limited imprints of plastic deformation, whereas the calcite grains in this domain preserve evidence of having undergone substantial viscous flow and strain localization due to diffusion creep. Our results show that reducing fluids such as H_2 can lead to pronounced strain localization without any substantial variations in the prevailing stress regime, by inducing phase transformations in carbonates. Lastly, our results suggest substantial reactivity between carbonates and H_2 at PT conditions relevant for subduction zone settings, and experiments should be performed to understand if such reactivity persists at lower PT conditions, before large-scale underground hydrogen storage (UHS) applications are pursued in carbonate reservoirs.

ACKNOWLEDGMENTS

The authors would like to thank David Iacopini and an anonymous reviewer whose critical inputs improved the manuscript. Mihai Ducea and an associate editor are thanked for their efficient editorial handling. This work is part of the project that has received funding from the European Research Council (ERC) under the European Union's Horizon 2020 research and innovation program to AVB (Grant Agreement No. 864045, acronym DeepSeep. A MUR FARE (grant No. R20ZJYMPAR, acronym DRYNK) grant and a MUR PRIN2022 (Grant No. 20224YR3AZ; acronym HYDECARB) to AVB are also acknowledged. Davide Cavalletti and Thomas Gusmeo are thanked for their help with Raman analyses and cathodoluminescence imaging, respectively.

REFERENCES CITED

Anders, M.H., Laubach, S.E., and Scholz, C.H., 2014, Microfractures: A review: Journal of Structural Geology, v. 69, p. 377–394, doi:10.1016/J.JSG.2014.05.011.

Anderson, O., and Grew, P.C., 1977, Stress corrosion theory of crack propagation with applications to geophysics: Reviews of Geophysics, v. 15, p. 77–104, doi:10.1029/RG015i001p00077.

Atkinson, B.K., 1984, SUBCRITICAL CRACK GROWTH IN GEOLOGICAL MATERIALS., *in* Journal of Geophysical Research, v. 89, p. 4077–4114, doi:10.1029/jb089ib06p04077.

Austrheim, H., 2013, Fluid and deformation induced metamorphic processes around Moho beneath continent collision zones: Examples from the exposed root zone of the Caledonian mountain belt, W-Norway: Tectonophysics, v. 609, p. 620–635, doi:10.1016/J.TECTO.2013.08.030.

Bachmann, F., Hielscher, R., and Schaeben, H., 2010, Texture analysis with MTEX- Free and open source software toolbox, *in* Solid State Phenomena, Trans Tech Publications Ltd, v. 160, p. 63–68, doi:10.4028/www.scientific.net/SSP.160.63.

Barber, D.J., Heard, H.C., and Wenk, H.R., 1981, Deformation of dolomite single crystals from 20-800° C: Physics and Chemistry of Minerals, v. 7, p. 271–286, doi:10.1007/BF00311980/METRICS.

Barber, D.J., and Wenk, H.R., 1979, Deformation twinning in calcite, dolomite, and other rhombohedral carbonates: Physics and Chemistry of Minerals, v. 5, p. 141–165, doi:10.1007/BF00307550/METRICS.

Barber, D.J., Wenk, H.R., and Heard, H.C., 1994, The plastic deformation of polycrystalline dolomite: comparison of experimental results with theoretical predictions: Materials Science and Engineering: A, v. 175, p. 83–104, doi:10.1016/0921-5093(94)91048-0.

Barnett, R.L., and Kerrich, R., 1980, Stress corrosion cracking of biotite and feldspar: Nature 1980 283:5743, v. 283, p. 185–187, doi:10.1038/283185a0.

Beltrando, M., Manatschal, G., Mohn, G., Dal Piaz, G.V., Vitale Brovarone, A., and Masini, E., 2014, Recognizing remnants of magma-poor rifted margins in high-pressure orogenic belts: The Alpine case study: Earth-Science Reviews, v. 131, p. 88–115, doi:10.1016/J.EARSCIREV.2014.01.001.

Berger, A., Ebert, A., Ramseyer, K., Gnos, E., and Decrouez, D., 2016, Dolomite microstructures between 390° and 700 °C: Indications for deformation mechanisms and grain size evolution: Journal of Structural Geology, v. 89, p. 144–152, doi:10.1016/J.JSG.2016.06.001.

Bestmann, M., and Prior, D.J., 2003, Intragranular dynamic recrystallization in naturally deformed calcite marble: Diffusion accommodated grain boundary sliding as a result of subgrain rotation recrystallization: Journal of Structural Geology, v. 25, p. 1597–1613, doi:10.1016/S0191-8141(03)00006-3.

Boutier, A., Martinez, I., Sissmann, O., Agostini, S., Daniel, I., Van Baalen, M., Mana, S., and Vitale Brovarone, A., 2024, Complexity of graphite formation in response to metamorphic methane generation and transformation in an orogenic ultramafic body: Geochimica et Cosmochimica Acta, v. 364, p. 166–183, doi:10.1016/J.GCA.2023.10.028.

Boutier, A., Vitale Brovarone, A., Martinez, I., Sissmann, O., and Mana, S., 2021, High-pressure serpentinization and abiotic methane formation in metaperidotite from the Appalachian subduction, northern Vermont: Lithos, v. 396–397, p. 106190, doi:10.1016/J.LITHOS.2021.106190.

Braid, H., Taylor, K., Hough, E., Rochelle, C., Niasar, V., and Ma, L., 2024, Hydrogen-induced mineral alteration: A review in the context of underground hydrogen storage (UHS) in saline aquifers: Earth-Science Reviews, v. 259, doi:10.1016/j.earscirev.2024.104975.

Brander, L., Svahnberg, H., and Piazolo, S., 2012, Brittle-plastic deformation in initially dry rocks at fluid-present conditions: transient behaviour of feldspar at mid-crustal levels: Contributions to Mineralogy and Petrology, v. 163, p. 403–425, doi:10.1007/s00410-011-0677-5.

Brantut, N., Heap, M.J., Meredith, P.G., and Baud, P., 2013, Time-dependent cracking and brittle creep in crustal rocks: A review: Journal of Structural Geology, v. 52, p. 17–43, doi:10.1016/j.jsg.2013.03.007.

Brovarone, A.V., Groppo, C., Hetényi, G., Compagnoni, R., and Malavieille, J., 2011, Coexistence of lawsonite-bearing eclogite and blueschist: Phase equilibria modelling of Alpine Corsica

metabasalts and petrological evolution of subducting slabs: Journal of Metamorphic Geology, v. 29, p. 583–600, doi:10.1111/j.1525-1314.2011.00931.x.

Brunet, C., Monié, P., Jolivet, L., and Cadet, J.P., 2000, Migration of compression and extension in the Tyrrhenian Sea, insights from 40Ar/39Ar ages on micas along a transect from Corsica to Tuscany: Tectonophysics, v. 321, p. 127–155, doi:10.1016/S0040-1951(00)00067-6.

Burke, E.A.J., 2001, Raman microspectrometry of fluid inclusions: Lithos, v. 55, p. 139–158, doi:10.1016/S0024-4937(00)00043-8.

Charlou, J.L., Donval, J.P., Fouquet, Y., Jean-Baptiste, P., and Holm, N., 2002, Geochemistry of high H2 and CH4 vent fluids issuing from ultramafic rocks at the Rainbow hydrothermal field (36°14′N, MAR): Chemical Geology, v. 191, p. 345–359, doi:10.1016/S0009-2541(02)00134-1.

Cohen, C.R., Schweickert, R.A., and Odom, A.L., 1981, Age of emplacement of the schistes lustres nappe, Alpine Corsica: Tectonophysics, v. 73, p. 267–283, doi:10.1016/0040-1951(81)90218-3.

Compagnoni, R., Cossio, R., and Mellini, M., 2021, Raman anisotropy in serpentine minerals, with a caveat on identification: Journal of Raman Spectroscopy, v. 52, p. 1334–1345, doi:10.1002/JRS.6128.

Connolly, J.A.D., 2005, Computation of phase equilibria by linear programming: A tool for geodynamic modeling and its application to subduction zone decarbonation: Earth and Planetary Science Letters, v. 236, p. 524–541, doi:https://doi.org/10.1016/j.epsl.2005.04.033.

Delle Piane, C., Burlini, L., and Kunze, K., 2009, The influence of dolomite on the plastic flow of calcite: Rheological, microstructural and chemical evolution during large strain torsion experiments: Tectonophysics, v. 467, p. 145–166, doi:10.1016/J.TECTO.2008.12.022.

Dobe, R., Das, A., Mukherjee, R., and Gupta, S., 2021, Evaluation of grain boundaries as percolation pathways in quartz-rich continental crust using Atomic Force Microscopy: Scientific Reports, v. 11, p. 9831, doi:10.1038/s41598-021-89250-z.

Fagereng, Å., and Diener, J., 2014, Brittle-viscous deformation, slow slip and tremor: Article in Geophysical Research Letters, doi:10.1002/2014GL060433.

Franzolin, E., Schmidt, M.W., and Poli, S., 2011, Ternary Ca-Fe-Mg carbonates: Subsolidus phase relations at 3.5 GPa and a thermodynamic solid solution model including order/disorder: Contributions to Mineralogy and Petrology, v. 161, p. 213–227, doi:10.1007/S00410-010-0527-X/FIGURES/9.

Frezzotti, M.L., Tecce, F., and Casagli, A., 2012, Raman spectroscopy for fluid inclusion analysis: Journal of Geochemical Exploration, v. 112, p. 1–20, doi:10.1016/J.GEXPLO.2011.09.009.

Fusseis, F., Allsop, C., Gilgannon, J., Schrank, C., Harley, S., and Schlepütz, C.M., 2023, Strain shadow “megapores” in mid-crustal ultramylonites: Geology, v. 51, p. 748–752, doi:10.1130/G51128.1/5876743/G51128.PDF.

Fusseis, F., and Handy, M.R., 2008, Micromechanisms of shear zone propagation at the brittle–viscous transition: Journal of Structural Geology, v. 30, p. 1242–1253, doi:10.1016/J.JSG.2008.06.005.

Fusseis, F., Regenauer-Lieb, K., Liu, J., Hough, R.M., and De Carlo, F., 2009, Creep cavitation can establish a dynamic granular fluid pump in ductile shear zones: Nature, v. 459, p. 974–977, doi:10.1038/nature08051.

Galvez, M.E., Martinez, I., Beyssac, O., Benzerara, K., Agrinier, P., and Assayag, N., 2013, Metasomatism and graphite formation at a lithological interface in Malaspina (Alpine Corsica, France): Contributions to Mineralogy and Petrology 2013 166:6, v. 166, p. 1687–1708, doi:10.1007/S00410-013-0949-3.

Gelencsér, O., Árvai, C., Mika, L.T., Breitner, D., LeClair, D., Szabó, C., Falus, G., and Szabó-Krausz, Z., 2023, Effect of hydrogen on calcite reactivity in sandstone reservoirs: Experimental results compared to geochemical modeling predictions: Journal of Energy Storage, v. 61, p. 106737, doi:10.1016/J.EST.2023.106737.

Getsinger, A.J., Hirth, G., Stünitz, H., and Goergen, E.T., 2013, Influence of water on rheology and strain localization in the lower continental crust: Geochemistry, Geophysics, Geosystems, v. 14, p. 2247–2264, doi:https://doi.org/10.1002/ggge.20148.

Gill-Olivas, B., Telling, J., Skidmore, M., and Tranter, M., 2023, Abrasion of sedimentary rocks as a source of hydrogen peroxide and nutrients to subglacial ecosystems: Biogeosciences, v. 20, p. 929–943, doi:10.5194/bg-20-929-2023.

Giuntoli, F., Menegon, L., Siron, G., Cognigni, F., Leroux, H., Compagnoni, R., Rossi, M., and Vitale Brovarone, A., 2024, Methane-hydrogen-rich fluid migration may trigger seismic failure in subduction zones at forearc depths: Nature Communications 2024 15:1, v. 15, p. 1–16, doi:10.1038/s41467-023-44641-w.

Giuntoli, F., Vitale Brovarone, A., and Menegon, L., 2020, Feedback between high-pressure genesis of abiotic methane and strain localization in subducted carbonate rocks: Scientific Reports, v. 10, p. 9848, doi:10.1038/s41598-020-66640-3.

Goncalves, P., Poilvet, J.C., Oliot, E., Trap, P., and Marquer, D., 2016, How does shear zone nucleate? An example from the Suretta nappe (Swiss Eastern Alps): Journal of Structural Geology, v. 86, p. 166–180, doi:10.1016/J.JSG.2016.02.015.

Gratier, J.P., Renard, F., and Labaume, P., 1999, How pressure solution creep and fracturing processes interact in the upper crust to make it behave in both a brittle and viscous manner: Journal of Structural Geology, v. 21, p. 1189–1197, doi:10.1016/S0191-8141(99)00035-8.

Harada, H., and Tsujimori, T., 2024, Methane genesis within olivine-hosted fluid inclusions in dolomitic marble of the Hida Belt, Japan: Progress in Earth and Planetary Science, v. 11, doi:10.1186/s40645-024-00609-y.

Helpa, V., Rybacki, E., Abart, R., Morales, L.F.G., Rhede, D., Jeřábek, P., and Dresen, G., 2014, Reaction kinetics of dolomite rim growth: Contributions to Mineralogy and Petrology, v. 167, p. 1–14, doi:10.1007/S00410-014-1001-Y/FIGURES/10.

Hentschel, F., Trepmann, C.A., and Janots, E., 2019, Deformation of feldspar at greenschist facies conditions-the record of mylonitic pegmatites from the Pfunderer Mountains, Eastern Alps: Solid Earth, v. 10, p. 95–116, doi:10.5194/SE-10-95-2019.

Higgs, D. V, and Handin, J., 1959, EXPERIMENTAL DEFORMATION OF DOLOMITE SINGLE CRYSTALS: GSA Bulletin, v. 70, p. 245–278, doi:10.1130/0016-7606(1959)70[245:EDODSC]2.0.CO;2.

Hirschmann, M.M., Withers, A.C., Ardia, P., and Foley, N.T., 2012, Solubility of molecular hydrogen in silicate melts and consequences for volatile evolution of terrestrial planets: Earth and Planetary Science Letters, v. 345–348, p. 38–48, doi:10.1016/J.EPSL.2012.06.031.

Holland, T.B., Hudson, N.F.C., Powell, R., and Harte, B., 2013, New Thermodynamic Models and Calculated Phase Equilibria in NCFMAS for Basic and Ultrabasic Compositions through the Transition Zone into the Uppermost Lower Mantle: Journal of Petrology, v. 54, p. 1901–1920, doi:10.1093/PETROLOGY/EGT035.

Holland, T.J.B., and Powell, R., 2011, An improved and extended internally consistent thermodynamic dataset for phases of petrological interest, involving a new equation of state for solids: Journal of Metamorphic Geology, v. 29, p. 333–383, doi:https://doi.org/10.1111/j.1525-1314.2010.00923.x.

Holyoke, C.W., Kronenberg, A.K., and Newman, J., 2013, Dislocation creep of polycrystalline dolomite: Tectonophysics, v. 590, p. 72–82, doi:10.1016/J.TECTO.2013.01.011.

Holyoke, C.W., Kronenberg, A.K., and Newman, J., 2014, Microstructural evolution during strain localization in dolomite aggregates: Journal of Structural Geology, v. 69, p. 449–464, doi:10.1016/J.JSG.2014.04.008.

Huang, J., Sverjensky, D.A., Daniel, I., and Vitale Brovarone, A., 2024, Reaction path model of the formation of abiotic immiscible hydrocarbon fluids in subducted carbonated serpentinites, Lanzo Massif (Western Italian Alps): Lithos, v. 468–469, doi:10.1016/j.lithos.2024.107498.

Imon, R., Okudaira, T., and Kanagawa, K., 2004, Development of shape- and lattice-preferred orientations of amphibole grains during initial cataclastic deformation and subsequent deformation by dissolution–precipitation creep in amphibolites from the Ryoke metamorphic belt, SW Japan: Journal of Structural Geology, v. 26, p. 793–805, doi:10.1016/J.JSG.2003.09.004.

Jolivet, L. et al., 1998, Midcrustal shear zones in postorogenic extension: Example from the northern Tyrrhenian Sea: Journal of Geophysical Research: Solid Earth, v. 103, p. 12123–12160, doi:10.1029/97JB03616.

Klein, F., Bach, W., and McCollom, T.M., 2013, Compositional controls on hydrogen generation during serpentinization of ultramafic rocks: Lithos, v. 178, p. 55–69, doi:10.1016/J.LITHOS.2013.03.008.

Kushnir, A.R.L., Kennedy, L.A., Misra, S., Benson, P., and White, J.C., 2015, The mechanical and microstructural behaviour of calcite-dolomite composites: An experimental investigation: Journal of Structural Geology, v. 70, p. 200–216, doi:10.1016/J.JSG.2014.12.006.

Lahondère, J.C., 1983, Carte géol. France (1/50000), feuille Bastia (1104).:

Lahondere, J.C., and Lahondere, D., 1988, The “schistes lustres’’, tectonic pile from Cap Corse[Organisation structurale des ‘schistes lustres’’ du Cap Corse (Haute- Corse)]’:” Comptes Rendus - Academie des Sciences, Serie II, v. 307, p. 1081–1086.

Lappan, R. et al., 2023, Molecular hydrogen in seawater supports growth of diverse marine bacteria: Nature Microbiology 2023 8:4, v. 8, p. 581–595, doi:10.1038/s41564-023-01322-0.

Lazar, C., Zhang, C., and Manning, C.E., 2014, Fluids in the crust. Redox effects on calcite-portlandite-fluid equilibria at for earc conditions: Carbon mobility, methanogenesis, and reduction melting of calcite: American Mineralogist, v. 99, p. 1604–1615, doi:10.2138/AM.2014.4696/MACHINEREADABLECITATION/RIS.

Li, J., Shao, T., Song, M., and Wang, H., 2021, Low-Temperature Plasticity and Dislocation Creep of Fangshan Dolomite: Journal of Geophysical Research: Solid Earth, v. 126, p. e2020JB021439, doi:10.1029/2020JB021439.

Lloyd, G.E., Farmer, A.B., and Mainprice, D., 1997, Misorientation analysis and the formation and orientation of subgrain and grain boundaries: Tectonophysics, v. 279, p. 55–78, doi:10.1016/S0040-1951(97)00115-7.

Lollar, B.S., Onstott, T.C., Lacrampe-Couloume, G., and Ballentine, C.J., 2014, The contribution of the Precambrian continental lithosphere to global H2 production: Nature 2014 516:7531, v. 516, p. 379–382, doi:10.1038/nature14017.

López Freixes, M., Zhou, X., Zhao, H., Godin, H., Peguet, L., Warner, T., and Gault, B., 2022, Revisiting stress-corrosion cracking and hydrogen embrittlement in 7xxx-Al alloys at the near-atomic-scale: Nature Communications 2022 13:1, v. 13, p. 1–9, doi:10.1038/s41467-022-31964-3.

Lopez-Sanchez, M.A., Tommasi, A., Ismail, W. Ben, and Barou, F., 2021, Dynamic recrystallization by subgrain rotation in olivine revealed by electron backscatter diffraction: Tectonophysics, v. 815, p. 228916, doi:10.1016/J.TECTO.2021.228916.

Malavieille, J., Chemenda, A., and Larroque, C., 1998, Evolutionary model for Alpine Corsica: Mechanism for ophiolite emplacement and exhumation of high-pressure rocks: Terra Nova, v. 10, p. 317–322, doi:10.1046/J.1365-3121.1998.00208.X.

Malki, M.L., Chellal, H., Mao, S., Rasouli, V., and Mehana, M., 2024, A critical review of underground hydrogen storage: From fundamentals to applications, unveiling future frontiers in energy storage: International Journal of Hydrogen Energy, v. 79, p. 1365–1394, doi:10.1016/j.ijhydene.2024.07.076.

Malusà, M.G., Faccenna, C., Baldwin, S.L., Fitzgerald, P.G., Rossetti, F., Balestrieri, M.L., Danišík, M., Ellero, A., Ottria, G., and Piromallo, C., 2015, Contrasting styles of (U)HP rock exhumation along the Cenozoic Adria-Europe plate boundary (Western Alps, Calabria, Corsica): Geochemistry, Geophysics, Geosystems, v. 16, p. 1786–1824, doi:10.1002/2015GC005767.

Malvoisin, B., Chopin, C., Brunet, F., and Galvez, M.E., 2012, Low-temperature Wollastonite Formed by Carbonate Reduction: a Marker of Serpentinite Redox Conditions: Journal of Petrology, v. 53, p. 159–176, doi:10.1093/PETROLOGY/EGR060.

Martin, L.A.J., Rubatto, D., Vitale Brovarone, A., and Hermann, J., 2011, Late Eocene lawsonite-eclogite facies metasomatism of a granulite sliver associated to ophiolites in Alpine Corsica: Lithos, v. 125, p. 620–640, doi:10.1016/J.LITHOS.2011.03.015.

McGlynn, S.E., Glass, J.B., Johnson-Finn, K., Klein, F., Sanden, S.A., Schrenk, M.O., Ueno, Y., and Vitale-Brovarone, A., 2020, Hydrogenation reactions of carbon on Earth: Linking methane, margarine, and life: American Mineralogist, v. 105, p. 599–608, doi:10.2138/AM-2020-6928CCBYNCND/ASSET/GRAPHIC/J_AM-2020-6928CCBYNCND_FIG_005.JPG.

Menegon, L., Fusseis, F., Stünitz, H., and Xiao, X., 2015, Creep cavitation bands control porosity and fluid flow in lower crustal shear zones: Geology, doi:10.1130/G36307.1.

Menegon, L., Stünitz, H., Nasipuri, P., Heilbronner, R., and Svahnberg, H., 2013, Transition from fracturing to viscous flow in granulite facies perthitic feldspar (Lofoten, Norway): Journal of Structural Geology, v. 48, p. 95–112, doi:10.1016/J.JSG.2012.12.004.

Michałowski, T., and Asuero, A.G., 2012, Thermodynamic modelling of dolomite behavior in aqueous media: Journal of Thermodynamics, v. 1, doi:10.1155/2012/723052.

Michalske, T.A., and Freiman, S.W., 1982, A molecular interpretation of stress corrosion in silica: Nature, v. 295, p. 511–512, doi:10.1038/295511a0.

Milesi, V., Guyot, F., Brunet, F., Richard, L., Recham, N., Benedetti, M., Dairou, J., and Prinzhofer, A., 2015, Formation of CO2, H2 and condensed carbon from siderite dissolution in the 200–300 °C range and at 50 MPa: Geochimica et Cosmochimica Acta, v. 154, p. 201–211, doi:10.1016/J.GCA.2015.01.015.

Molli, G., 2008, Northern Apennine-Corsica orogenic system: An updated overview: Geological Society Special Publication, v. 298, p. 413–442, doi:10.1144/SP298.19.

Molli, G., and Malavieille, J., 2011, Orogenic processes and the Corsica/Apennines geodynamic evolution: Insights from Taiwan: International Journal of Earth Sciences, v. 100, p. 1207–1224, doi:10.1007/S00531-010-0598-Y/FIGURES/7.

Molli, G., Menegon, L., and Malasoma, A., 2017, Switching deformation mode and mechanisms during subduction of continental crust: a case study from Alpine Corsica: Solid Earth, v. 8, p. 767–788, doi:10.5194/se-8-767-2017.

Moore, J., Piazolo, S., Beinlich, A., Austrheim, H., and Putnis, A., 2024, Brittle initiation of dissolution–precipitation creep in plagioclase-rich rocks: insights from the Bergen arcs, Norway: Contributions to Mineralogy and Petrology, v. 179, p. 1–18, doi:10.1007/S00410-024-02141-0/FIGURES/8.

Morales, L.F.G., 2022, Interphase misorientation as a tool to study metamorphic reactions and crystallization in geological materials: American Mineralogist, v. 107, p. 1501–1518, doi:10.2138/AM-2021-7902.

Newman, J., and Mitra, G., 1994, Fluid-influenced deformation and recrystallization of dolomite at low temperatures along a natural fault zone, Mountain City window, Tennessee: GSA Bulletin, v. 106, p. 1267–1280, doi:10.1130/0016-7606(1994)106<1267:FIDARO>2.3.CO;2.

Nicolas, A., Fortin, J., Regnet, J.B., Dimanov, A., and Güeguen, Y., 2016, Brittle and semi-brittle behaviours of a carbonate rock: influence of water and temperature: Geophysical Journal International, v. 206, p. 438–456, doi:10.1093/GJI/GGW154.

Osselin, F., Soulaine, C., Fauguerolles, C., Gaucher, E.C., Scaillet, B., and Pichavant, M., 2022, Orange hydrogen is the new green: Nature Geoscience, v. 15, p. 765–769, doi:10.1038/s41561-022-01043-9.

Passchier, C.W., and Trouw, R.A.J., 2005, Microtectonics: Springer Berlin Heidelberg, 1–366 p., doi:10.1007/3-540-29359-0.

Pearce, M.A., Timms, N.E., Hough, R.M., and Cleverley, J.S., 2013, Reaction mechanism for the replacement of calcite by dolomite and siderite: Implications for geochemistry, microstructure and porosity evolution during hydrothermal mineralisation: Contributions to Mineralogy and Petrology, v. 166, p. 995–1009, doi:10.1007/S00410-013-0905-2/FIGURES/7.

Peña-Alvarez, M., Brovarone, A.V., Donnelly, M.E., Wang, M., Dalladay-Simpson, P., Howie, R., and Gregoryanz, E., 2021, In-situ abiogenic methane synthesis from diamond and graphite under geologically relevant conditions: Nature Communications 2021 12:1, v. 12, p. 1–5, doi:10.1038/s41467-021-26664-3.

Peng, W., Zhang, L., Tumiati, S., Vitale Brovarone, A., Hu, H., Cai, Y., and Shen, T., 2021, Abiotic methane generation through reduction of serpentinite-hosted dolomite: Implications for carbon mobility in subduction zones: Geochimica et Cosmochimica Acta, v. 311, p. 119–140, doi:10.1016/J.GCA.2021.07.033.

Pennacchioni, G., and Mancktelow, N.S., 2007, Nucleation and initial growth of a shear zone network within compositionally and structurally heterogeneous granitoids under amphibolite facies conditions: Journal of Structural Geology, v. 29, p. 1757–1780, doi:10.1016/J.JSG.2007.06.002.

Perrillat, J.-P., Daniel, I., Koga, K.T., Reynard, B., Cardon, H., and Crichton, W.A., 2005, Kinetics of antigorite dehydration: A real-time X-ray diffraction study:, doi:10.1016/j.epsl.2005.06.006.

Peverelli, V., Olivieri, O.S., Tsujimori, T., Giovannelli, D., Shi, G., Cannaò, E., Piccoli, F., and Vitale Brovarone, A., 2024, Cold-subduction biogeodynamics boosts deep energy delivery to the forearc: Geochimica et Cosmochimica Acta, doi:10.1016/j.gca.2024.10.004.

Post, A., and Tullis, J., 1998, The rate of water penetration in experimentally deformed quartzite: Implications for hydrolytic weakening: Tectonophysics, v. 295, p. 117–137.

Précigout, J., Prigent, C., Palasse, L., and Pochon, A., 2017, Water pumping in mantle shear zones: Nature Communications, v. 8, p. 1–10, doi:10.1038/ncomms15736.

Prinzhofer, A., Rigollet, C., Lefeuvre, N., Françolin, J., and Valadão de Miranda, P.E., 2024, Maricá (Brazil), the new natural hydrogen play which changes the paradigm of hydrogen exploration: International Journal of Hydrogen Energy, v. 62, p. 91–98, doi:10.1016/J.IJHYDENE.2024.02.263.

Prinzhofer, A., Tahara Cissé, C.S., and Diallo, A.B., 2018, Discovery of a large accumulation of natural hydrogen in Bourakebougou (Mali): International Journal of Hydrogen Energy, v. 43, p. 19315–19326, doi:10.1016/J.IJHYDENE.2018.08.193.

Putnis, C. V., Tsukamoto, K., and Nishimura, Y., 2005, Direct observations of pseudomorphism: Compositional and textural evolution at a fluid-solid interface: American Mineralogist, v. 90, p. 1909–1912, doi:10.2138/AM.2005.1990/MACHINEREADABLECITATION/RIS.

Ravna, E.J.K., Andersen, T.B., Jolivet, L., and de Capitani, C., 2010, Cold subduction and the formation of lawsonite eclogite - constraints from prograde evolution of eclogitized pillow lava from Corsica: Journal of Metamorphic Geology, v. 28, p. 381–395, doi:10.1111/J.1525-1314.2010.00870.X.

Reber, J.E., and Pec, M., 2018, Comparison of brittle- and viscous creep in quartzites: Implications for semi-brittle flow of rocks: Journal of Structural Geology, v. 113, p. 90–99, doi:10.1016/j.jsg.2018.05.022.

Reeves, E.P., and Seewald, J.S., 2024, Hydrothermal carbon reduction in the absence of minerals: Geochimica et Cosmochimica Acta, v. 381, p. 60–74, doi:10.1016/j.gca.2024.07.024.

Renard, F., 2021, Reaction-Induced Fracturing: When Chemistry Breaks Rocks: Journal of Geophysical Research: Solid Earth, v. 126, doi:10.1029/2020JB021451.

Robertson, I.M., Sofronis, P., Nagao, A., Martin, M.L., Wang, S., Gross, D.W., and Nygren, K.E., 2015, Hydrogen Embrittlement Understood: Metallurgical and Materials Transactions A: Physical Metallurgy and Materials Science, v. 46, p. 2323–2341, doi:10.1007/S11661-015-2836-1/METRICS.

Di Rosa, M., Farina, F., Lanari, P., and Marroni, M., 2020a, Pre-Alpine thermal history recorded in the continental crust from Alpine Corsica (France): evidence from zircon and allanite LA-ICP-MS dating: Swiss Journal of Geosciences 2020 113:1, v. 113, p. 1–22, doi:10.1186/S00015-020-00374-2.

Di Rosa, M., Frassi, C., Marroni, M., Meneghini, F., and Pandolfi, L., 2020b, Did the "Autochthonous" European foreland of Corsica Island (France) experience Alpine subduction? Terra Nova, v. 32, p. 34–43, doi:10.1111/TER.12433.

Di Rosa, M., Meneghini, F., Marroni, M., Frassi, C., and Pandolfi, L., 2020c, The coupling of high-pressure oceanic and continental units in Alpine Corsica: Evidence for syn-exhumation tectonic erosion at the roof of the plate interface: Lithos, v. 354–355, p. 105328, doi:10.1016/J.LITHOS.2019.105328.

Rossetti, F., Cavazza, W., Di Vincenzo, G., Lucci, F., and Theye, T., 2023, Alpine tectono-metamorphic evolution of the Corsica basement: Journal of Metamorphic Geology, v. 41, p. 299–326, doi:10.1111/JMG.12696.

Rossi, P., Lahondère, J.C., Lluch, D., and Loÿle-Pilot, M.D., 1994, Carte géol. France (1/50000), feuille Saint Florent (1103).:

Ruiz-Agudo, E., Putnis, C. V., and Putnis, A., 2014, Coupled dissolution and precipitation at mineral-fluid interfaces: Chemical Geology, v. 383, p. 132–146, doi:10.1016/j.chemgeo.2014.06.007.

Rutter, E.H., and Brodie, K.H., 1995, Mechanistic interactions between deformation and metamorphism: Geological Journal, v. 30, p. 227–240, doi:10.1002/GJ.3350300304.

Sack, R.O., and Ghiorso, M.S., 1991, Chromian spinels as petrogenetic indicators: Thermodynamics and petrological applications.:

Schenk, O., and Urai, J.L., 2005, The migration of fluid-filled grain boundaries in recrystallizing synthetic bischofite: first results of in-situ high-pressure, high-temperature deformation

experiments in transmitted light: Journal of Metamorphic Geology, v. 23, p. 695–709, doi:10.1111/J.1525-1314.2005.00604.X.

Schwartz, S., Guillot, S., Reynard, B., Lafay, R., Debret, B., Nicollet, C., Lanari, P., and Auzende, A.L., 2013, Pressure–temperature estimates of the lizardite/antigorite transition in high pressure serpentinites: Lithos, v. 178, p. 197–210, doi:10.1016/J.LITHOS.2012.11.023.

Scully, J.R., Young, G.A., and Smith, S.W., 2012, Hydrogen embrittlement of aluminum and aluminum-based alloys: Gaseous Hydrogen Embrittlement of Materials in Energy Technologies: The Problem, its Characterisation and Effects on Particular Alloy Classes, p. 707–768, doi:10.1533/9780857093899.3.707.

Skemer, P., Katayama, I., Jiang, Z., and Karato, S.I., 2005, The misorientation index: Development of a new method for calculating the strength of lattice-preferred orientation: Tectonophysics, v. 411, p. 157–167, doi:10.1016/j.tecto.2005.08.023.

Skemer, P., Katayama, I., and Karato, S.I., 2006, Deformation fabrics of the Cima di Gagnone peridotite massif, Central Alps, Switzerland: Evidence of deformation at low temperatures in the presence of water: Contributions to Mineralogy and Petrology, v. 152, p. 43–51, doi:10.1007/S00410-006-0093-4.

Sleep, N.H., Meibom, A., Fridriksson, T., Coleman, R.G., and Bird, D.K., 2004, H2-rich fluids from serpentinization: Geochemical and biotic implications: Proceedings of the National Academy of Sciences of the United States of America, v. 101, p. 12818–12823, doi:10.1073/PNAS.0405289101/ASSET/A49E3DE1-FED7-40CC-B5DE-BF5AEBDE0EE9/ASSETS/GRAPHIC/ZPQ0350458700004.JPEG.

Spruzeniece, L., Piazolo, S., and Maynard-Casely, H.E., 2017, Deformation-resembling microstructure created by fluid-mediated dissolution–precipitation reactions: Nature Communications 2017 8:1, v. 8, p. 1–9, doi:10.1038/ncomms14032.

Su, Q., Zeller, E., and Angino, E., 1992, Inducing action of hydrogen migrating along faults on earthquakes: Acta Seismologica Sinica, v. 5, p. 841–847, doi:10.1007/BF02651032/METRICS.

Tao, R., Zhang, L., Tian, M., Zhu, J., Liu, X., Liu, J., Höfer, H.E., Stagno, V., and Fei, Y., 2018, Formation of abiotic hydrocarbon from reduction of carbonate in subduction zones: Constraints from petrological observation and experimental simulation: Geochimica et Cosmochimica Acta, v. 239, p. 390–408, doi:10.1016/J.GCA.2018.08.008.

Trepmann, C.A., and Stöckhert, B., 2003, Quartz microstructures developed during non-steady state plastic flowat rapidly decaying stress and strain rate: Journal of Structural Geology, v. 25, p. 2035–2051, doi:10.1016/S0191-8141(03)00073-7.

Truche, L., Donzé, F.V., Goskolli, E., Muceku, B., Loisy, C., Monnin, C., Dutoit, H., and Cerepi, A., 2024, A deep reservoir for hydrogen drives intense degassing in the Bulqizë ophiolite: Science, v. 383, p. 618–621, doi:10.1126/SCIENCE.ADK9099/SUPPL_FILE/SCIENCE.ADK9099_MOVIE_S1.ZIP.

Viola, G., Mancktelow, N.S., and Miller, J.A., 2006, Cyclic frictional-viscous slip oscillations along the base of an advancing nappe complex: Insights into brittle-ductile nappe emplacement mechanisms from the Naukluft Nappe Complex, central Namibia: Tectonics, v. 25, doi:10.1029/2005TC001939.

Vitale Brovarone, A., Beltrando, M., Malavieille, J., Giuntoli, F., Tondella, E., Groppo, C., Beyssac, O., and Compagnoni, R., 2011, Inherited Ocean–Continent Transition zones in deeply subducted terranes: Insights from Alpine Corsica: Lithos, v. 124, p. 273–290, doi:10.1016/J.LITHOS.2011.02.013.

Vitale Brovarone, A., Beyssac, O., Malavieille, J., Molli, G., Beltrando, M., and Compagnoni, R., 2013, Stacking and metamorphism of continuous segments of subducted lithosphere in a high-pressure wedge: The example of Alpine Corsica (France): Earth-Science Reviews, v. 116, p. 35–56, doi:10.1016/J.EARSCIREV.2012.10.003.

Vitale Brovarone, A., and Herwartz, D., 2013, Timing of HP metamorphism in the Schistes Lustrés of Alpine Corsica: New Lu–Hf garnet and lawsonite ages: Lithos, v. 172–173, p. 175–191, doi:10.1016/J.LITHOS.2013.03.009.

Vitale Brovarone, A., Martinez, I., Elmaleh, A., Compagnoni, R., Chaduteau, C., Ferraris, C., and Esteve, I., 2017, Massive production of abiotic methane during subduction evidenced in metamorphosed ophicarbonates from the Italian Alps: Nature Communications, v. 8, p. 14134, doi:10.1038/ncomms14134.

Vitale Brovarone, A., Picatto, M., Beyssac, O., Lagabrielle, Y., and Castelli, D., 2014, The blueschist–eclogite transition in the Alpine chain: P–T paths and the role of slow-spreading extensional structures in the evolution of HP–LT mountain belts: Tectonophysics, v. 615–616, p. 96–121, doi:10.1016/J.TECTO.2014.01.001.

Vitale Brovarone, A., Sverjensky, D.A., Piccoli, F., Ressico, F., Giovannelli, D., and Daniel, I., 2020, Subduction hides high-pressure sources of energy that may feed the deep subsurface biosphere: Nature Communications 2020 11:1, v. 11, p. 1–11, doi:10.1038/s41467-020-17342-x.

Whitney, D.L., and Evans, B.W., 2010, Abbreviations for names of rock-forming minerals: American Mineralogist, v. 95, p. 185–187, doi:10.2138/am.2010.3371.

Woodtli, J., and Kieselbach, R., 2000, Damage due to hydrogen embrittlement and stress corrosion cracking: Engineering Failure Analysis, v. 7, p. 427–450, doi:10.1016/S1350-6307(99)00033-3.

Yoshida, K., Okamoto, A., Shimizu, H., Oyanagi, R., and Tsuchiya, N., 2020, Fluid Infiltration Through Oceanic Lower Crust in Response to Reaction-Induced Fracturing: Insights From Serpentinized Troctolite and Numerical Models: Journal of Geophysical Research: Solid Earth, v. 125, p. e2020JB020268, doi:10.1029/2020JB020268.

Zertani, S., Morales, L.F.G., and Menegon, L., 2024, Omphacite breakdown: nucleation and deformation of clinopyroxene-plagioclase symplectites: Contributions to Mineralogy and Petrology, v. 179, doi:10.1007/s00410-024-02125-0.

Zhang, L., Qi, N., Li, Y., Wang, X., and Zhang, L., 2024, Immiscible metamorphic water and methane fluids preserved in carbonated eclogite: Communications Chemistry, v. 7, doi:10.1038/s42004-024-01355-4.

FIGURE CAPTIONS

Figure 1. Geological setting of the study area. A) Map showing the distribution of peak Alpine metamorphic conditions in Alpine Corsica modified after Vitale Brovarone et al. (2013). The study area is highlighted with a red star. B) Lithological map of the study area and its surroundings showing the broad distribution of rock types, modified after Rossi et al. (1994) and Lahondère (1983).

Figure 2. Structural setting of the Negru Shear Zone. A) Panoramic view of the Negru Shear Zone. B) Sketch of the first-order structural arrangement of the Negru Shear Zone. C) Photo of the studied segment of the Negru Shear Zone (GPS coordinates: 42.76328ºN, 9.338714ºE) with major structural elements highlighted. D) Sketch of the outcrop shown in C, illustrating the structural relationships between different generations of veins, graphitized deformation bands and the main foliation within the serpentinite.

Figure 3. Examples of carbonate distribution and transformations on the upper serpentinite block of the Negru Shear Zone (see Fig. 2 C-D for location of panels A-B, C-D and E-F). In the legend, carbonate refers to mixed dolomite and calcite-bearing domains and for carbonate+graphite bearing domains, the shading in the legend is indicative of the relative abundance of graphite (darker shades reflect higher abundance). A) Extensive, chaotic network of dolomite-rich veins (yellow/brown) transected by a later stage calcite vein (white). B) Interpretative sketch of the structural relationships of A. C) Brecciated and partially reacted (calcite + graphite) dolomite vein cross-cutting the host serpentinite. The locations of samples COR18-7a and 7b are shown black boxes. D) Sketch of the structural relationships of C. Note the calcite vein cross-cutting both the serpentinite and the deformation band. E) Strongly graphitized deformation band within serpentinite. Truncated calcite veins are drawn into parallelism with the band, suggesting their involvement in the activity of the deformation band. F) Sketch of the structural elements of E. G) Slab of layered domains preserving different degrees of reaction, from partially reacted, brecciated dolomite to a fully homogenized layer composed of dolomite + graphite. An intermediate layer of carbonate+graphite+serpentinite clasts is also observed. The locations of sample 3COR19-20Zb and 20Zc are shown in black boxes. H) Sketch of the

1242 structural elements of G. Note the pods of the brecciated dolomite in the lowermost carbonate-
1243 rich horizon.
1244 Figure 4. Thin-section photomicrographs and cathodoluminescence intensity maps. Yellow
1245 boxes correspond to the textural domains shown in greater detail in Fig. 5 and green boxes
1246 correspond to domains from which the BSE images in Fig. 6 and the EBSD maps in Figs. 9-11
1247 were acquired. Mineral abbreviations from Whitney and Evans (2010). A) Cross-polarized
1248 photomicrograph of the host serpentinite (COR18-7b). B) Cross-polarized photomicrograph of a
1249 brecciated dolomite pod (COR18-7a) within a graphitized deformation band from the Negru
1250 Shear Zone. C) Cathodoluminescence intensity map of COR18-7a. Brighter domains correspond
1251 to calcite-rich domains, darker domains correspond to dolomite-rich domains. The serpentinite
1252 clasts are black. D-F) Cross-polarized photomicrograph (D&F) and cathodoluminescence
1253 intensity map (E) of interface between serpentinite and carbonate vein (3COR19-20Zb&c; See
1254 Fig. 3G for sample locations). The thin sections are flipped horizontally with respect to their
1255 schematic positions shown in Fig. 3G.
1256 Figure 5. Microphotographs of the representative microstructural domains highlighted with
1257 yellow and green boxes in Fig. 4. A) Foliated serpentine from the host serpentinite (COR18-7b).
1258 A kink band is observable with the trace of the axial plane normal to the foliation. B) Brecciated
1259 fragments of twinned dolomite (COR18-7a) containing twins of variable widths. The fragments
1260 are lined by graphite, magnetite and calcite. C) Relict twinned dolomite grain surrounded by a
1261 recrystallized matrix of finer-grained dolomite (3COR19-20Zb). This domain corresponds to
1262 domain 1 (dolomite-rich high-strain zone) of the EBSD-based textural analyses presented in
1263 Section 3.3 below. D) Recrystallized carbonate in association with porphyroclasts of the host
1264 serpentinite (3COR19-20Zb). E) Relict, twinned dolomite grains surrounded by a matrix of fine-

grained dolomite with an intervening fringe of calcite, graphite and magnetite (3COR19-20Zb). This domain corresponds to domain 2 (zone of incipient calcite formation) of the EBSD-based textural analyses presented in Section 3.3. EDS maps of this domain are shown in Figs. 7E-H. F) Calcite, graphite and magnetite at junctions between brecciated fragments of twinned dolomite (COR18-7a). G) Transition between relict, twinned dolomite and highly recrystallized calcite in domains of advanced calcite formation (COR18-7a). This domain corresponds to domain 3 (zone of advanced calcite formation) of the EBSD-based textural analyses presented in Section 3.3. EDS maps of this domain have been presented in Figs. 7I-L. H) Sheared diopside layer crosscut by late-stage carbonate veins (3COR19-20Zc).

Figure 6. BSE images of representative textural domains. A) Incipient growth of calcite at the intersection between brecciated dolomite fragments (see Figs. 4B&C and 5F for precise location of the domain). B) Fine-grained dolomite (see Figs. 4B&C for domain correlation). Individual grains of dolomite become progressively darker from core to rim, corresponding to a decrease in Fe/Mg ratio due to Fe loss. EDS maps from this domain have been presented in Figs. 7A-D. C) Fringe of incipient calcite growing onto twinned dolomite, in association with graphite and magnetite, transitioning laterally into a domain of recrystallized dolomite (see Figs. 4D&E and 5E for domain correlation). D) Domain of advanced calcite formation within which fragments of dolomite are observed to be completely engulfed within zones of calcite growth (see Figs. 4D&E for domain correlation).

Figure 7. EDS maps of distributions of Ca, Mg and Fe from representative textural domains. The brightness in each map is directly correlated with the abundance of the element. A-D) High-strain, fine-grained, dolomite-rich domain from COR18-7a. The location of this domain is shown in Figs. 4B&C (green box corresponding to Fig. 6B) and detailed microstructural relationships

have been described in Fig. 6B. Note the increase in Mg at the margins of the dolomite fragments corresponding to a decrease in the Fe content. E-H) domain of incipient calcite formation from 3COR19-20Zb. The location of this domain has been highlighted in Figs. 4D&E (green box corresponding to Figs. 5E and 6C), and the microstructural relationships have been described in Figs. 5E&6C. I-L) Domain of advanced calcite formation from COR18-7a. The location of this domain is shown in Figs. 4B&C (green box corresponding to Fig. 5G), and detailed microstructural relationships have been described in Fig. 5G. Inclusions of unreacted dolomite are engulfed within the calcite-rich layer (J&K).

Figure 8. Representative Raman spectra of species of interest. A) photomicrograph of fluid inclusion trails and clusters within brecciated dolomite. B) Raman spectra of the fluid inclusion highlighted with an arrow in A. Enhanced view of characteristic peaks for H_2 in the inset. C) photomicrograph of fluid inclusions within relict twinned and brecciated fragment of dolomite inside a high-strain domain. D) Raman spectra of the fluid inclusion highlighted with an arrow in C. Enhanced view of characteristic peaks for H_2 in the inset. E) photomicrograph of fluid inclusion trail within calcite from the domains of advanced calcite formation. F) Raman spectra of the fluid inclusion highlighted with an arrow in E. Enhanced view of characteristic peaks for H_2 in the inset. G) Plane-polarized photomicrograph of a diopside grain with fluid inclusions. H) Raman spectra obtained from a fluid inclusion highlighted with a black arrow in (G), with representative Raman peaks for diopside. CH_4 and H_2 highlighted. Note the presence of CH_4 in B, F and H and its absence in D. Mineral abbreviations from Whitney and Evans (2010).

Figure 9. EBSD maps and pole figures from high strain domains (domain 1) consisting of fine-grained dolomite and no calcite. (A) GROD map. The white line transecting the relict dolomite grain in the center corresponds to the misorientation profile shown in B. (B) GROD map with

misorientation profile in the inset. Cumulative misorientations (misorientation at a point relative to the misorientation at the first point) and point-to-point misorientations (misorientation at each point) are shown as red and blue curves, respectively. (C) Neighbor pair (blue) and random pair (yellow) misorientation angle distribution. (D) Pole figures of dolomite.

Figure 10. EBSD maps and pole figures from domains of incipient calcite formation (domain 2) consisting of relict and fine-grained dolomite along with calcite at the interface between the relict and fine-grained dolomite domains. (A) GROD map (B&C) Neighbor pair (blue) and random pair (yellow) misorientation angle distributions of dolomite and calcite respectively. (D) Pole figures of dolomite (top) and calcite (bottom). (E) Map of interphase misorientations between calcite and dolomite.

Figure 11. EBSD maps and pole figures from domains of advanced calcite formation (domain 3) consisting of relict, twinned grains of dolomite adjacent to domain consisting of fine-grained calcite engulfing isolated grains of dolomite. (A) GROD map (B&C) Neighbor pair (blue) and random pair (yellow) misorientation angle distributions of dolomite and calcite respectively. (D) Pole figures of dolomite (top) and calcite (bottom). (E) Map of interphase misorientations between calcite and dolomite.

Figure 12. Thermodynamic modeling at 1 GPa. A) pseudosection. B) dolomite proportions (mol%) in dolomite. C) ankerite proportions (mol%) in dolomite. D) relative amount of Ca in carbonates.

Figure 13. Thermodynamic modeling at 2 GPa. A) Pseudosection. B) Dolomite proportions (mol%) in dolomite. C) Ankerite proportions (mol%) in dolomite. D) Relative amount of Ca in carbonates.

Figure 14. Schematic diagram depicting the progressive transformation of initial coarse-grained dolomite in yellow to fine grained Ca-carbonate+graphite in grey with increasing H_2 infiltration over time.

TABLE CAPTIONS

Table 1. Qualitative and quantitative micro-Raman spectroscopy results on six pre-selected fluid inclusions from the NSZ area. The table includes host mineral, fluid composition based on Raman analysis, CH_4 (v1) and H_2 (Q1(1)) Raman shifts (expressed in cm-1), CH_4 and H_2 peak areas, and molar fractions in the gas phase (expressed in mol%). The peak areas were computed after subtraction of a linear baseline. The CH_4 and H_2 molar fractions were calculated using their respective peak areas and Raman scattering cross-sections reported by (Burke, 2001) for a green 514 nm laser.

[1]Supplemental Material. *[Materials supplementary to the manuscript]* Please visit https://doi.org/10.1130/gsab.s.29189777 to access the supplemental material, and contact editing@geosociety.org with any questions.

1349 Fig. 1

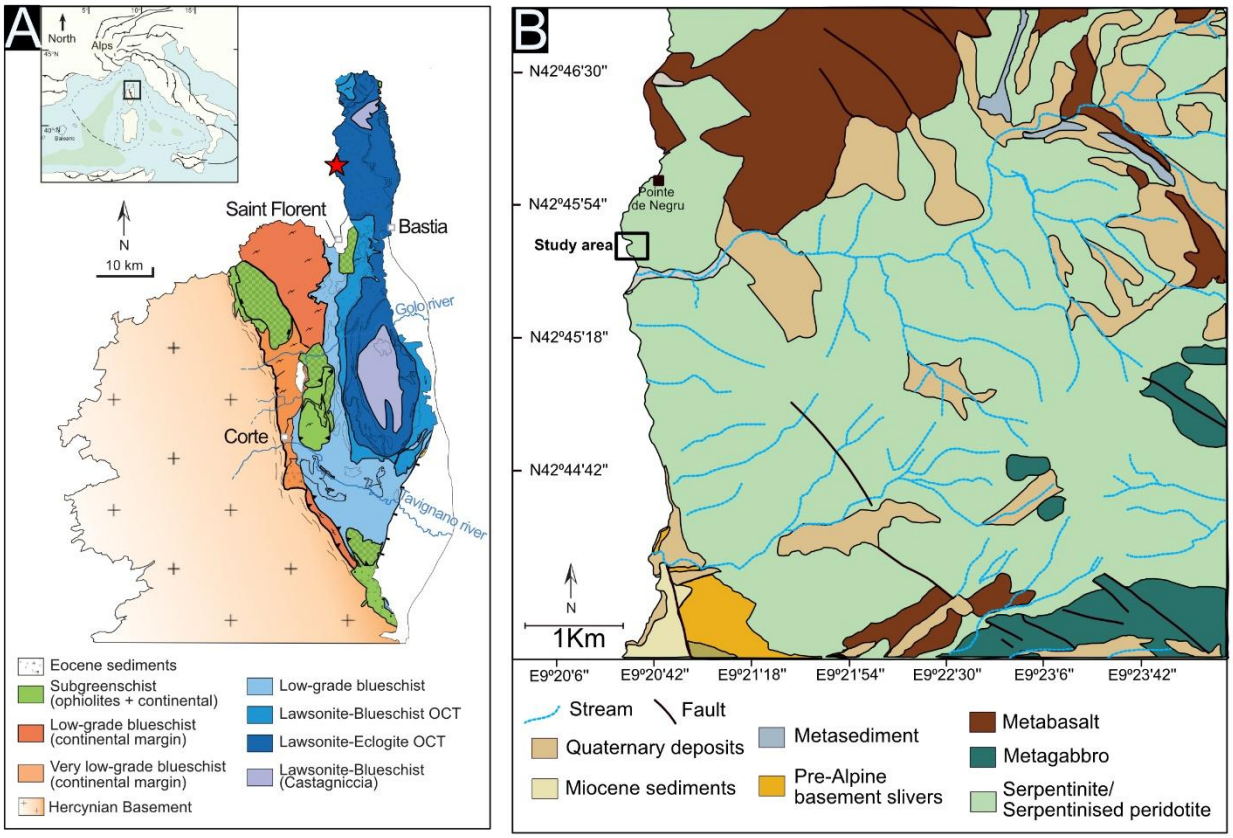

1350
1351
1352

1353 Fig. 2

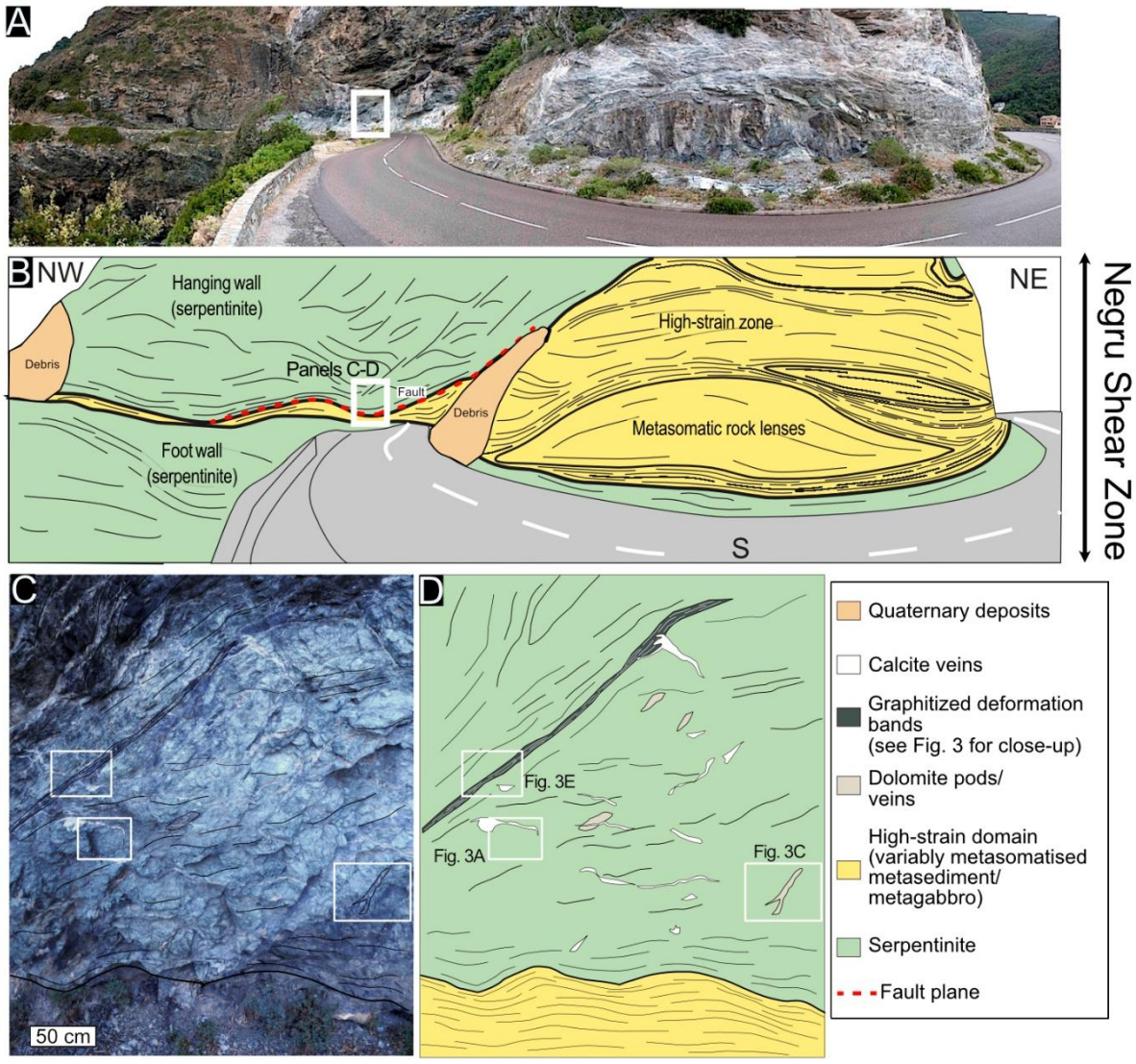

1354
1355

1356

Fig. 3

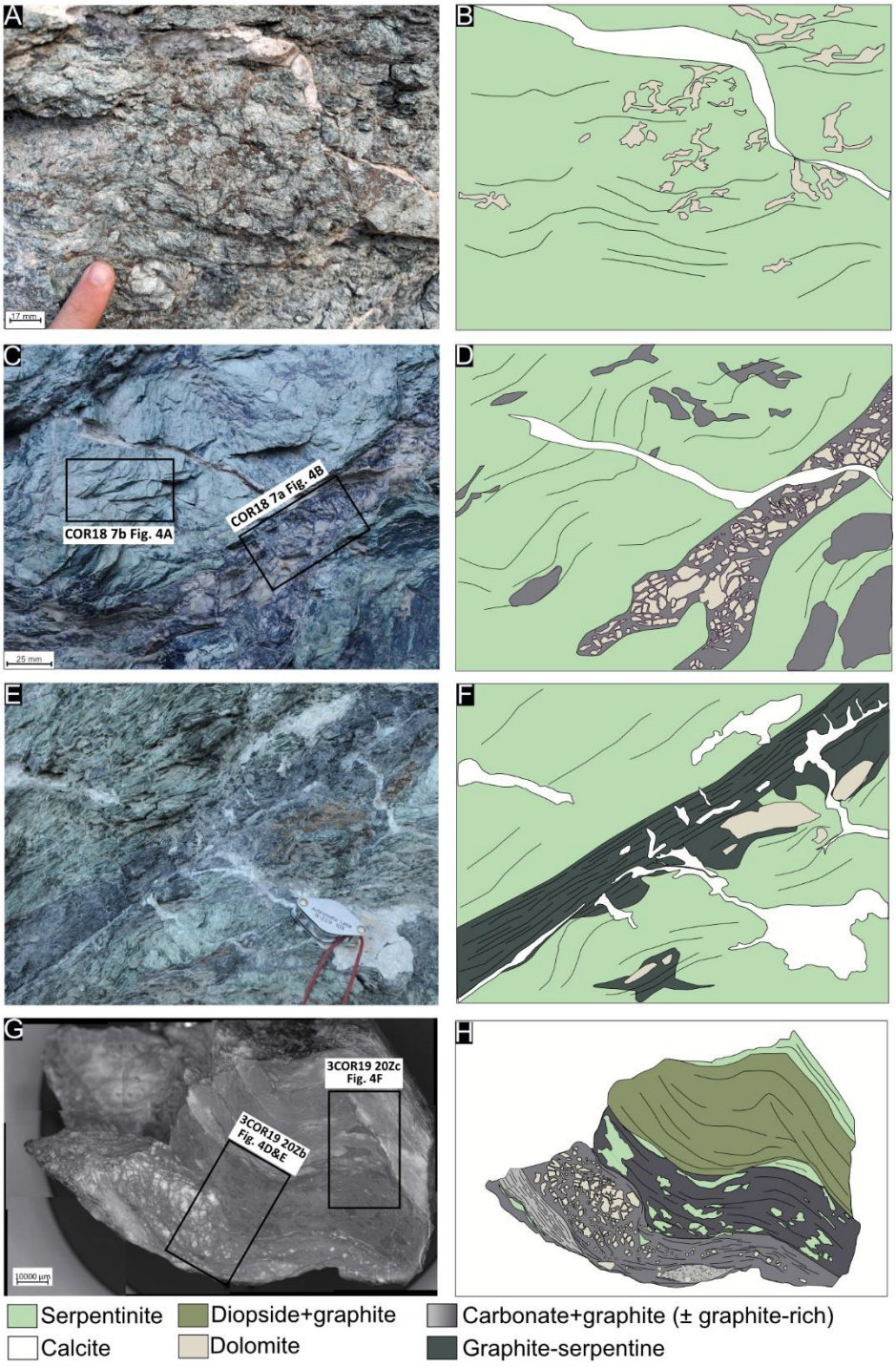

1357
1358

Fig. 4

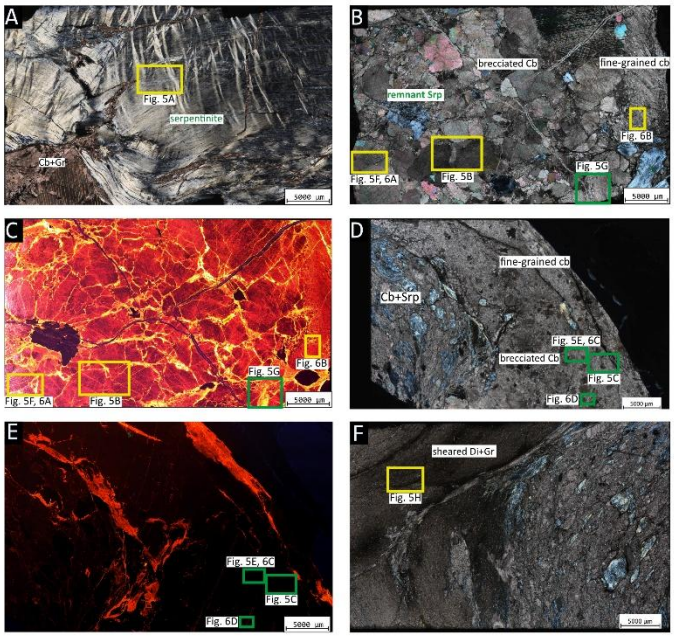
A
Fig. 5A
serpentinite
Cb+Gr
5000 µm
B
brecciated Cb
fine-grained cb
remnant Srp
Fig. 6B
Fig. 5F, 6A
Fig. 5B
Fig. 5G
5000 µm
C
Fig. 6B
Fig. 5G
Fig. 5F, 6A
Fig. 5B
5000 µm
D
fine-grained cb
Cb+Srp
Fig. 5E, 6C
brecciated Cb
Fig. 5C
Fig. 6D
3000 µm
E
Fig. 5E, 6C
Fig. 5C
Fig. 6D
5000 µm
F
sheared Di+Gr
Fig. 5H
5000 µm

1362

Fig. 5

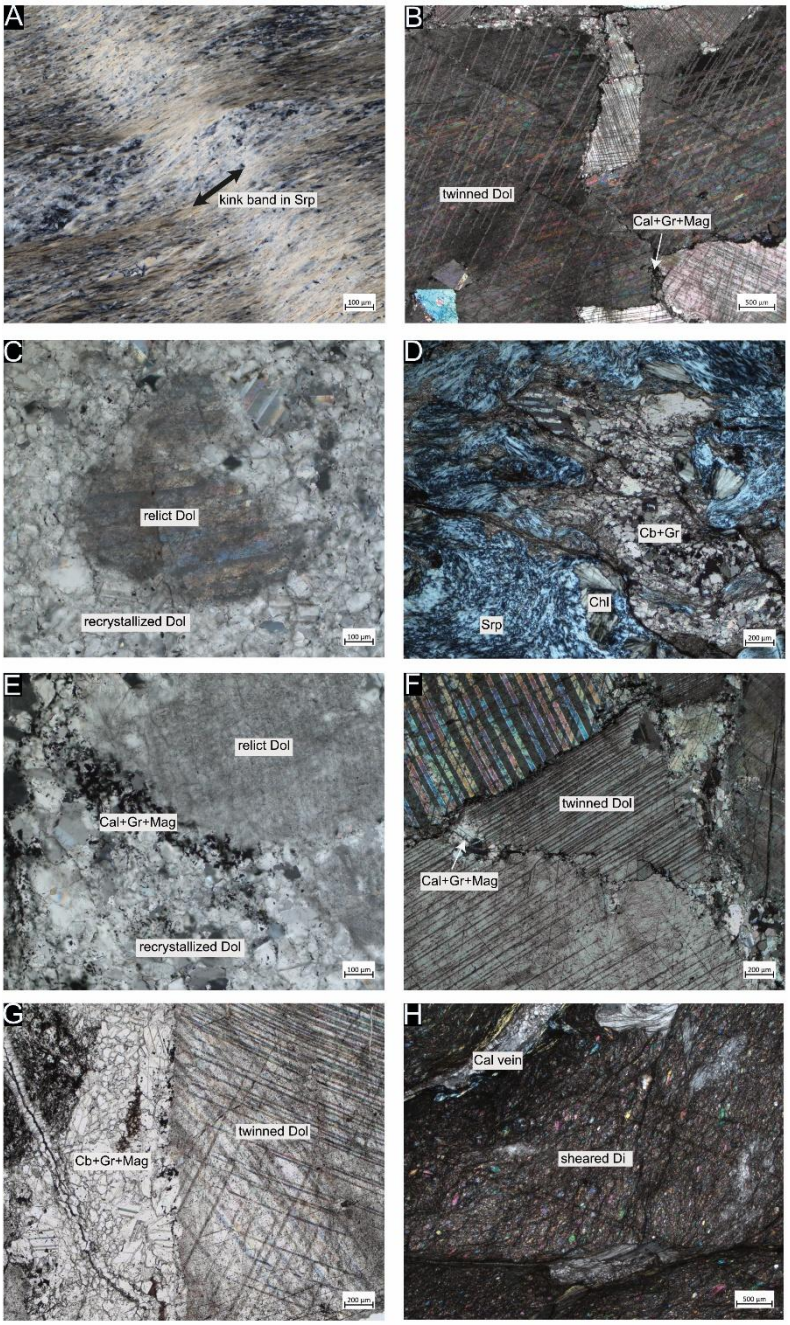

1363
1364

1365 Fig. 6

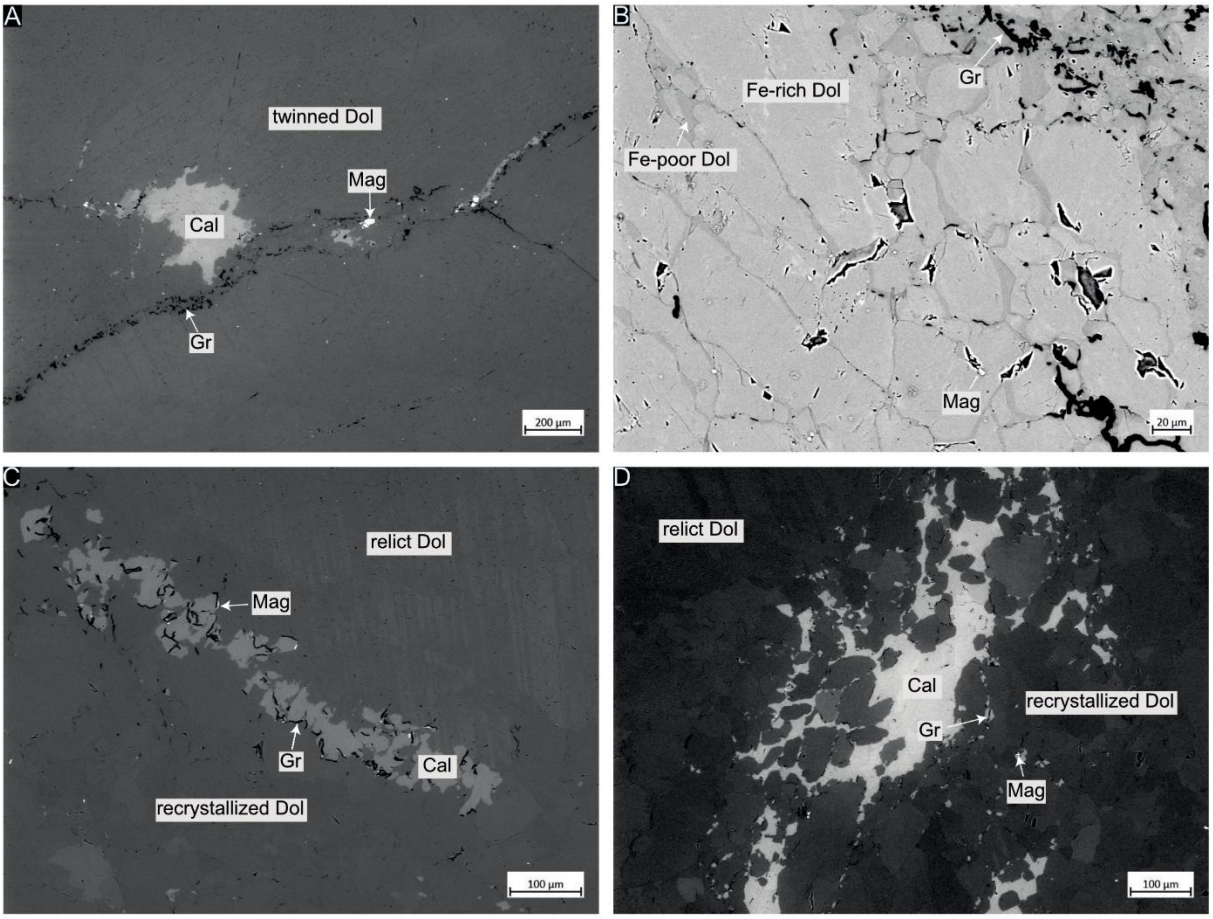

1366
1367

1368

Fig. 7

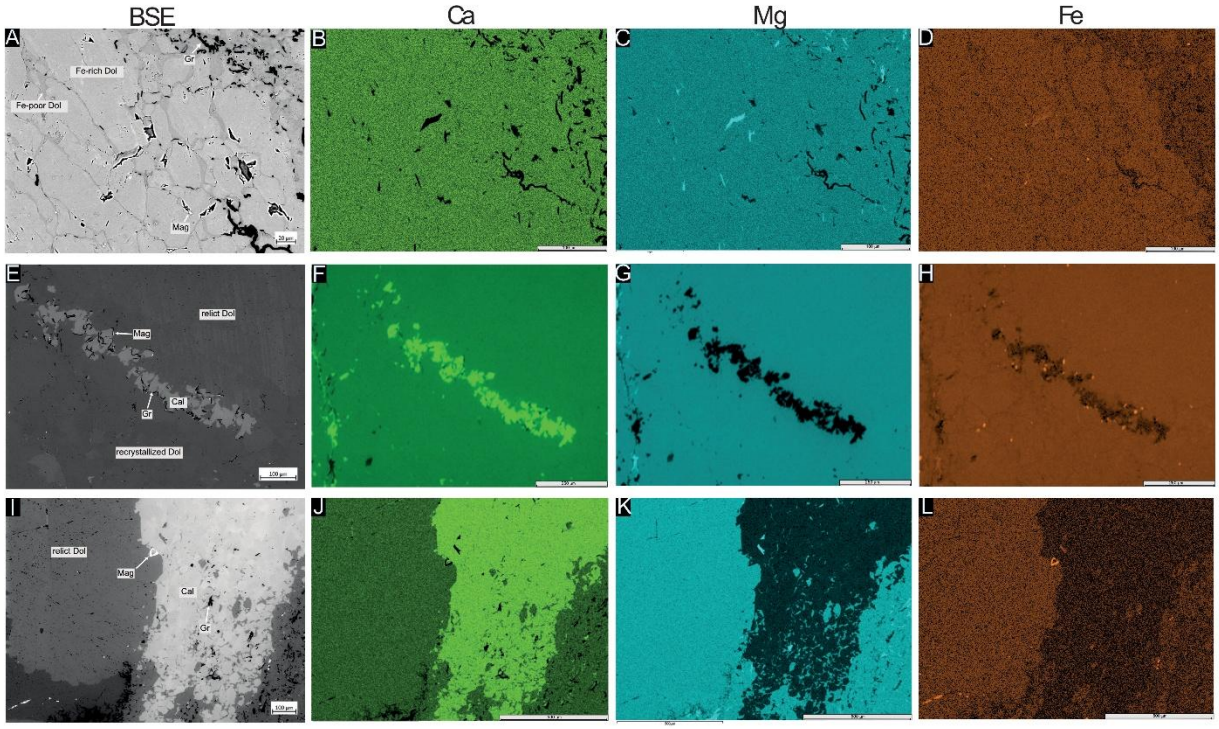

1369
1370

1371

Fig. 8

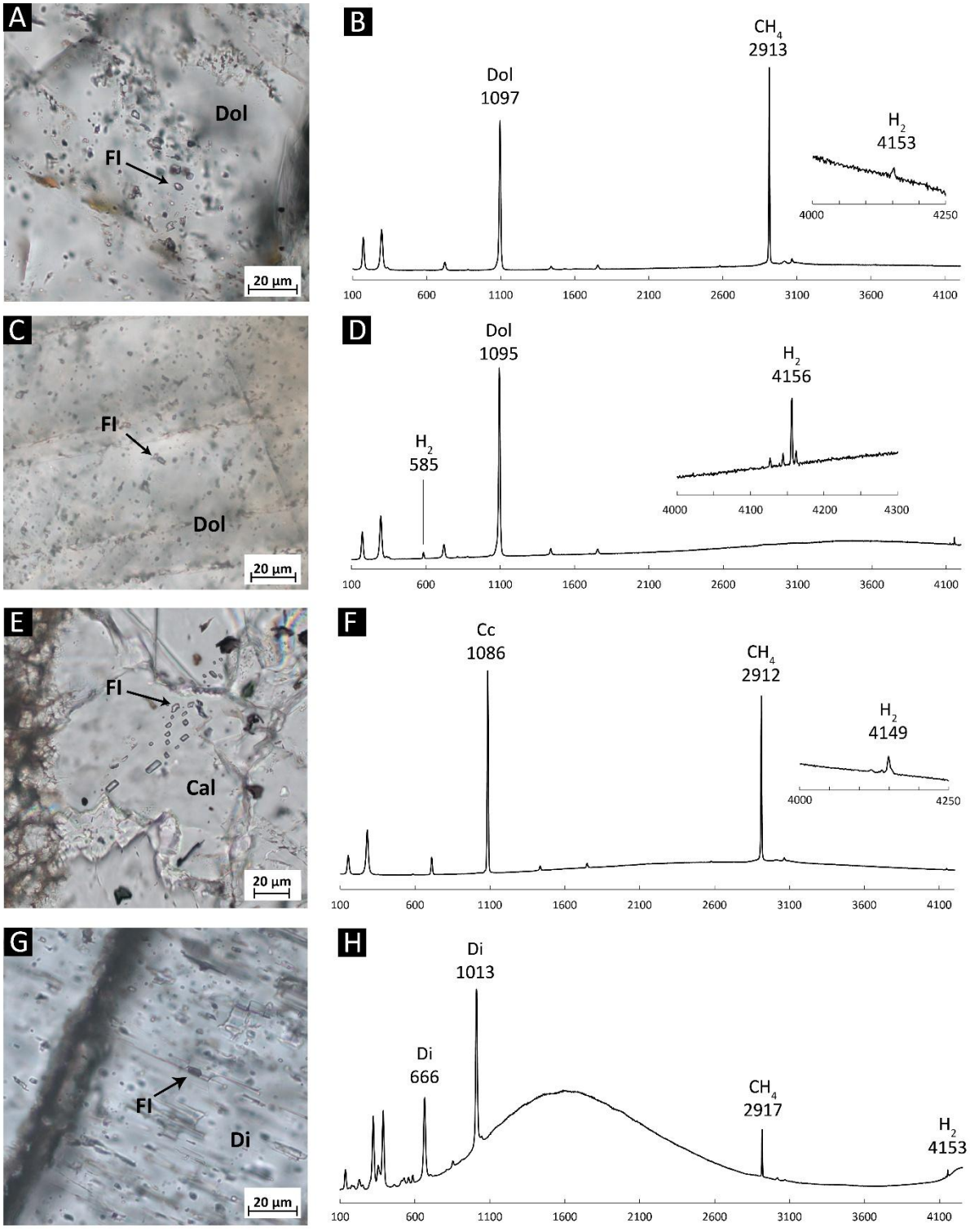

1372
1373

1374

Fig. 9

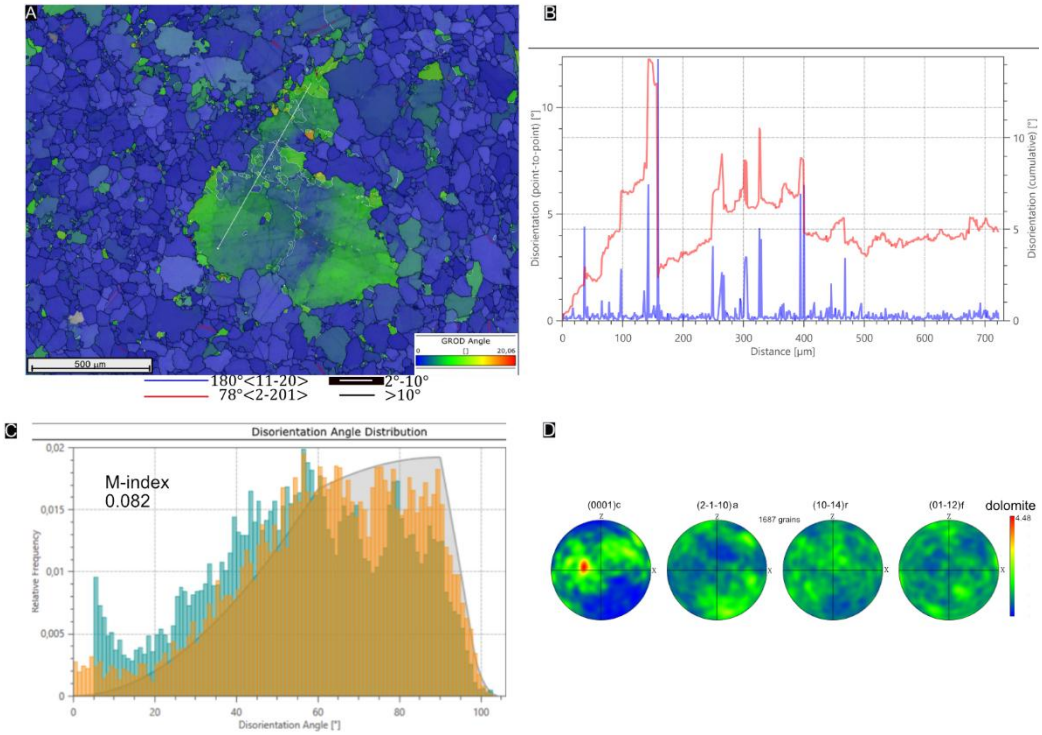

1375
1376

1377 Fig. 10

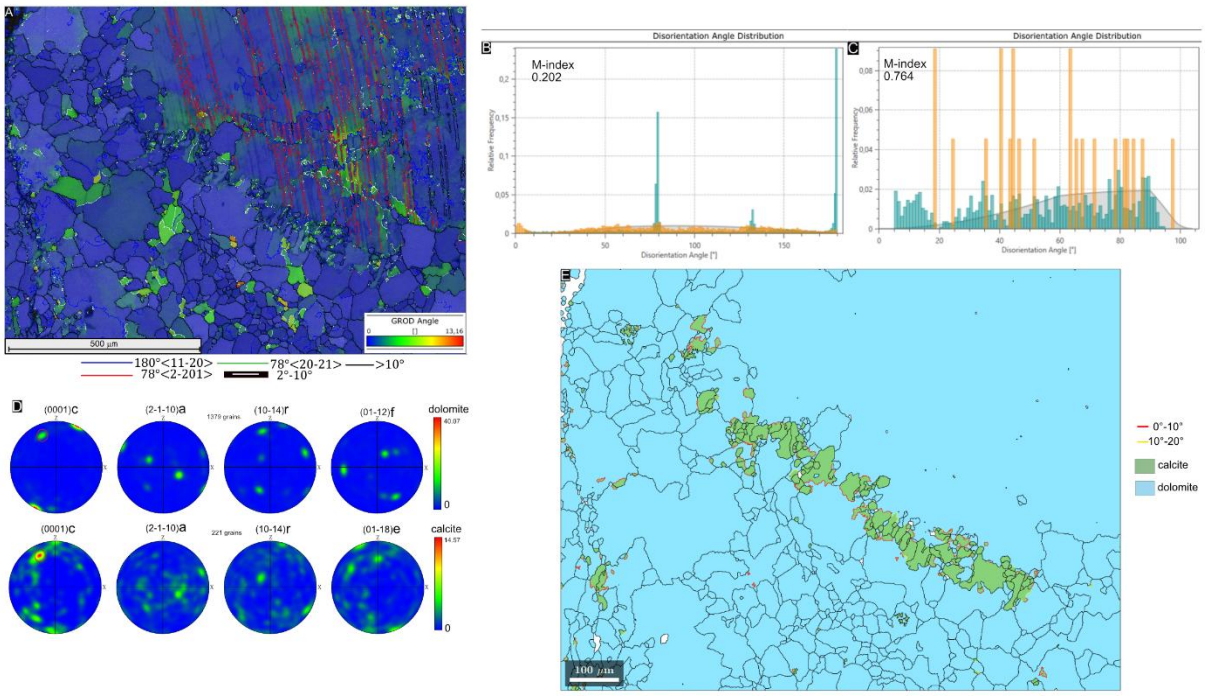

1378
1379

1380

Fig. 11

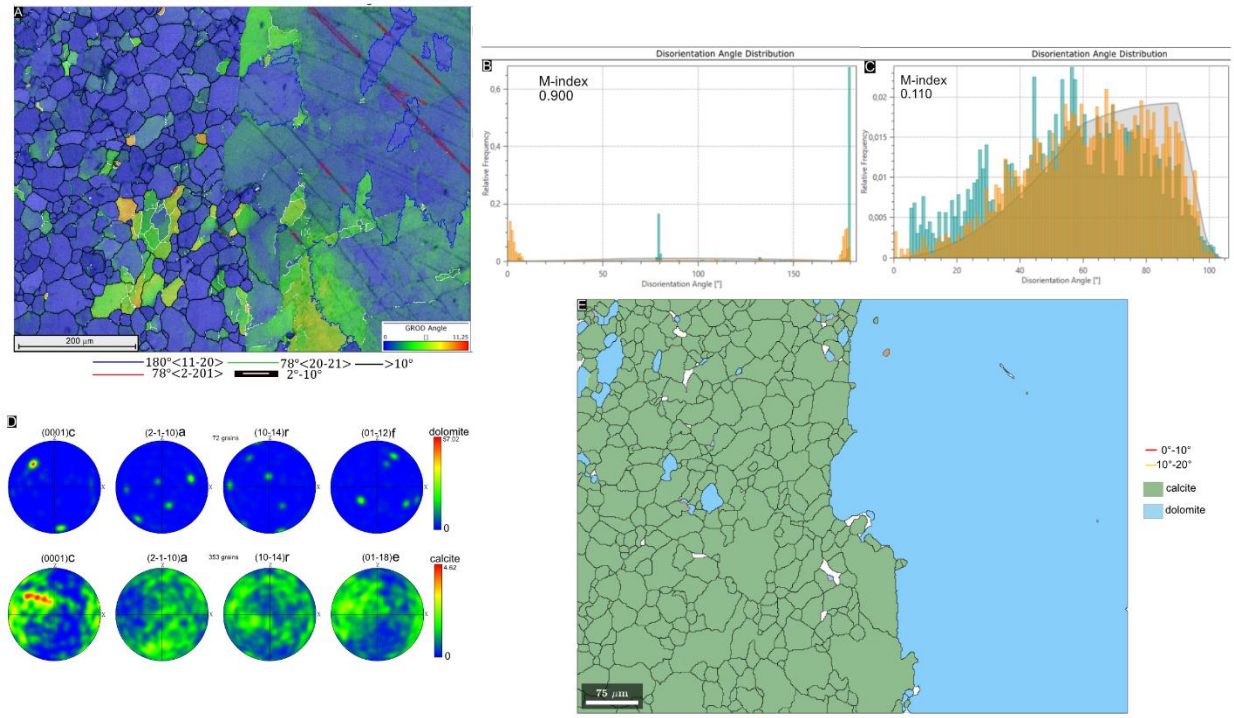

1381
1382

1383

Fig. 12

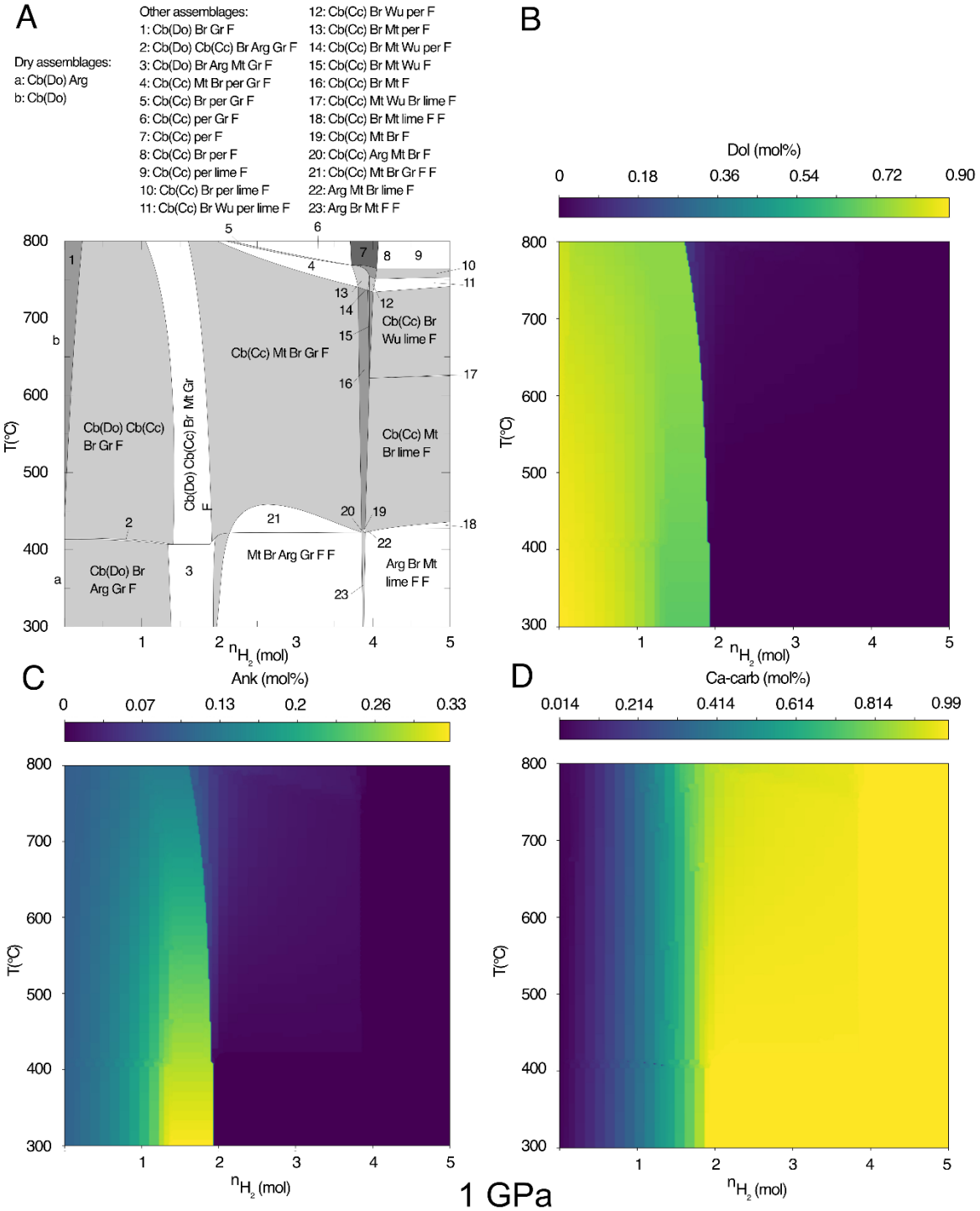

1384
1385

1386

Fig. 13

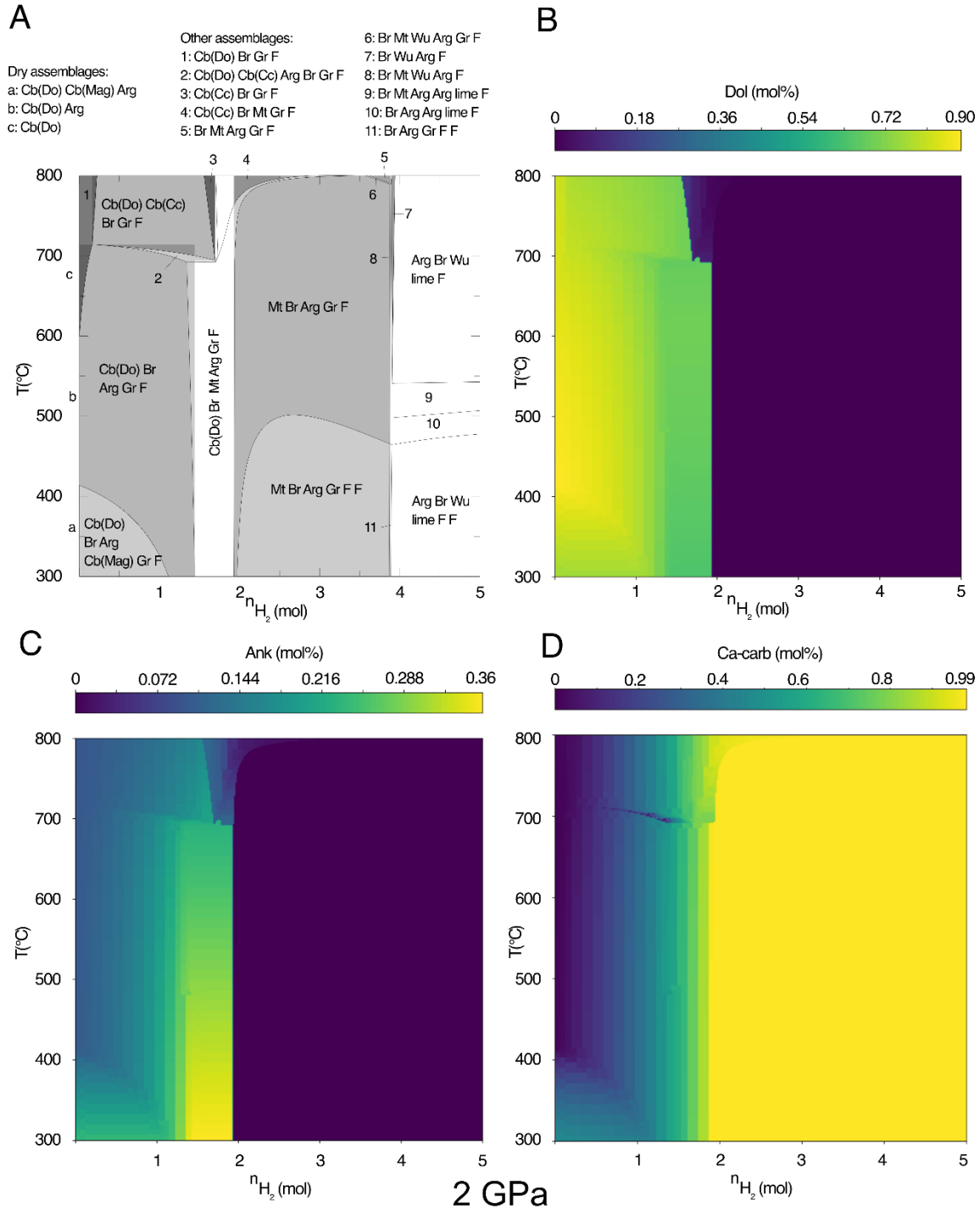

1387
1388

1389 Fig. 14

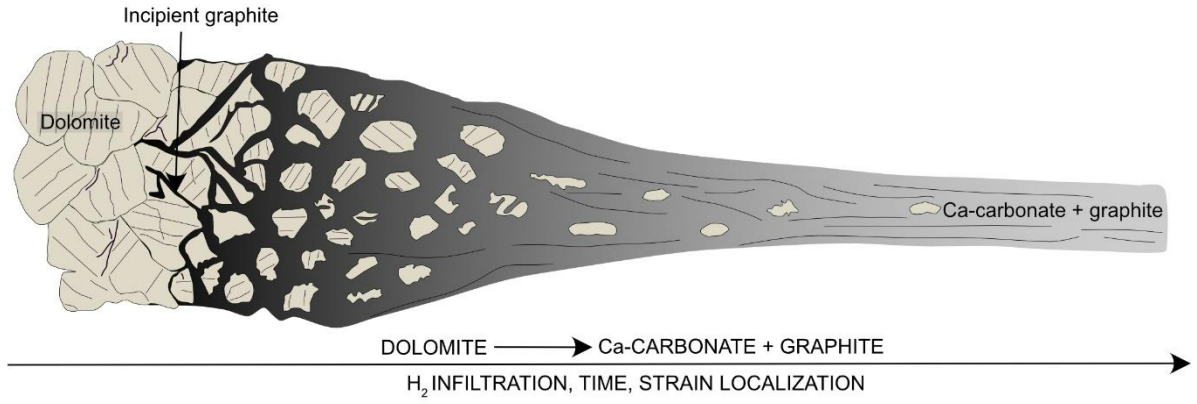

1390